BROADBAND SPECTRAL SPLITTING OF LIGHT USING WAVEFRONT SHAPING

A THESIS SUBMITTED TO
THE GRADUATE SCHOOL OF NATURAL AND APPLIED SCIENCES
OF
MIDDLE EAST TECHNICAL UNIVERSITY

BY

YALIN BAŞAY

IN PARTIAL FULFILLMENT OF THE REQUIREMENTS
FOR
THE DEGREE OF MASTER OF SCIENCE
IN
MICRO AND NANOTECHNOLOGY

AUGUST 2018

Approval of the thesis:

BROADBAND SPECTRAL SPLITTING OF LIGHT USING WAVEFRONT SHAPING

submitted by **YALIN BAŞAY** in partial fulfillment of the requirements for the degree of **Master of Science in Micro and Nanotechnology Department, Middle East Technical University** by,

Prof. Dr. Halil Kalıpçılar
Dean, Graduate School of **Natural and Applied Sciences** _____________________

Assoc. Prof. Dr. Burcu Akata Kurç
Head of Department, **Micro and Nanotechnology** _____________________

Asst. Prof. Dr. Emre Yüce
Supervisor, **Physics Dept., METU** _____________________

Asst. Prof. Dr. Selçuk Yerci
Co-Supervisor, **Micro and Nanotechnology, METU** _____________________

Examining Committee Members:

Asst. Prof. Dr. Onur Tokel
Physics Dept., Bilkent University _____________________

Asst. Prof. Dr. Emre Yüce
Physics Dept., METU _____________________

Prof. Dr. Mehmet Parlak
Physics Dept., METU _____________________

Assoc. Prof. Dr. Serhat Çakır
Physics Dept., METU _____________________

Asst. Prof. Dr. Ihor Pavlov
Physics Dept., METU _____________________

Date: 31.08.2018

I hereby declare that all information in this document has been obtained and presented in accordance with academic rules and ethical conduct. I also declare that, as required by these rules and conduct, I have fully cited and referenced all material and results that are not original to this work.

Name, Last name : Yalın Başay

Signature :

ABSTRACT

BROADBAND SPECTRAL SPLITTING OF LIGHT USING WAVEFRONT SHAPING

Başay, Yalın
M.Sc, Micro and Nanotechnology
Supervisor: Asst. Prof. Dr. Emre Yüce
Co-Supervisor: Asst. Prof. Dr. Selçuk Yerci

August 2018, 55 pages

Splitting of light to different frequencies is an important tool for several photonic research and applications. One of those applications is increasing the absorption of light via spectral splitting in solar energy systems. Nowadays, this splitting process is realized by fixed diffraction gratings. However, these structures can't adapt to the environmental changes and their efficiencies differ from season to season. A structure that can adapt to environmental changes would certainly increase the efficiency of solar energy systems. When the dimensions of a medium are comparable to wavelength of light, diffraction plays a major role in wave propagation and it differs by wavelength. Thus, it is possible to obtain intended phase difference for each frequency by changing the thickness or refractive index of the medium. As a result, waves at a specific frequency can be controlled to constructively interfere at a desired point. Liquid crystal displays, which enable to control refractive indices of each pixels via modulating the amplitude of the applied electric field can be used to control diffraction. By this programmable control, the spatial phase of light can be changed between 0-2π and the phase pattern for spectral splitting can be determined. As a result, light can be spectrally split using an adaptive medium. In this thesis, we will use liquid crystal displays to determine a micro structure that can achieve spectral splitting at different angles of incident light. In accordance with this purpose, spectral splitting of light will be customized to a region or a building. In addition, we will also investigate the effectiveness of the spectral splitting and the splitting ratio. Our spectral splitting patterns promise an increase in solar cell efficiency given that the effectiveness will be customized to the location where the solar cell will be positioned.

Keywords: Diffraction, Spectral Splitting, Solar Cells

ÖZ

DALGA ÖNÜ ŞEKİLLENDİRMESİ İLE GENİŞ BANT SPEKTRAL AYRIŞTIRMA

Başay, Yalın
Yüksek Lisans, Mikro ve Nanoteknoloji
Tez Yöneticisi : Dr. Öğr. Üyesi Emre Yüce
Ortak Tez Yôneticisi: Dr. Öğr. Üyesi Selçuk Yerci

Ağustos 2018, 55 sayfa

Işığın farklı dalga boylarına ayrılması fotonik alanındaki birçok uygulamada ve araştırmada önem taşımaktadır. Bu uygulamalardan biri, güneş enerjisi sistemleri için ışığın spektral olarak ayrıştırılıp daha verimli bir şekilde soğurulmasıdır. Günümüzde bu ayrıştırma işlemi ızgara benzeri mikro yapılar sayesinde gerçekleştirilmektedir. Ancak bu yapılar çevresel faktörlere uyum sağlayamadığı için verimlilikleri mevsimlere ve çevresel değişimlere göre farklılık göstermektedir. Yapıların çevresel değişimlere uyum sağlayabilmesi durumunda güneş enerjisi sistemlerinde kayda değer bir verim artışı olacaktır. Işığın dalga boyuyla karşılaştırılabilecek derecede küçük ortamlarda kırınım her bir dalga boyu için farklılık göstermektedir. Buradan yola çıkarak, ortamın kalınlığının veya kırılma indisinin değiştirilmesiyle her bir frekansta istenilen kadar faz kayması sağlanabilir ve böylece her bir frekanstaki ışığın yapıcı girişime uğradığı nokta kontrol edilebilir. Sıvı kristal ekranlar, uygulanan elektriksel alanın genliğine bağlı olarak her bir pikselin kırılma indisini kontrol etme imkânı sağladığından kırınım optik uygulamalarında kullanılabilir. Işık, bu prensibe dayalı çalışan SLM gibi kırınım optik elemanları sayesinde spektral olarak ayrıştırılabilmektedir. Bu çalışmada, sıvı kristal ekranlar kullanılarak ölçümlerin yapılması, verimliliği arttıran holografik yapıya karar verilmesi ve böylece gün veya yıl içerisinde verimliliği optimum seviyeye çıkaracak holografik yapıların belirlenmesi amaçlanmaktadır. Bu amaç doğrultusunda, uzaysal ışık modülatörleri kullanılarak ışığın spektral ayrışması programlanabilir olarak yapılacak ve bu ayrışmanın kullanılan frekans aralığında etkinliği ile ayrıştırma oranı incelenecektir. Bu sayede bölgelere veya binalara optimize edilmiş mikro yapılar belirlenebilecek, geniş bantta spektral ayrıştırma yapılarak güneş enerji sistemlerinde verimlilik artırılabilecektir.

Anahtar Kelimeler: Kırınım, Spektral Ayrıştırma, Güneş Panelleri

To those who struggle for a peaceful world,

even at the most brutal moment of war

ACKNOWLEDGMENTS

First of all, I would like to thank my advisor Asst. Prof. Dr. Emre Yüce and my co-advisor Asst. Prof. Dr. Selçuk Yerci for their guidance and support.

I would like to thank my thesis committee members Asst. Prof. Dr. Onur Tokel, Prof. Dr. Mehmet Parlak, Assoc. Prof. Dr. Serhat Çakır and Asst. Prof. Dr. Ihor Pavlov for their valuable feedback.

I would like to thank all past and current members of Programmable Photonics Group for their support and friendship at every stage of this work and my graduation.

Finally, I would like to thank my family and all of my friends for making my life livable.

TABLE OF CONTENTS

LIST OF FIGURES

FIGURES

CHAPTER 1

INTRODUCTION

Although the term “energy” was firstly used in its modern sense by Thomas Young in 1807, existence of humankind is dependent on what this term [1]. Human beings must persistently take energy from outside, generally in the form of food, which can be plants that convert energy of sun light to chemical energy by photosynthesis, or animals that feed on plants in order to survive and reproduce. Besides this biological process, extreme ability to manipulate surroundings, which includes potentiality of switching between energy types, provides an advantageous for human to stay alive. Learning to control fire, which is transformation of chemical energy stored in biomass to heat, is a milestone for human life since by this way early humans have been able to stay alive at low temperatures, improve their protection at nights and prevent illnesses caused by foods by cooking them [2]. However, after agricultural revolution, people have been obliged to find new energy sources as water and wind power because of the increment of human population [3]. Until the industrial revolution that began in the mid-18th century, these limited energy sources had been available, however it is the period of time when they started to be insufficient in consequence of the increase in energy usage. Finding out the significant amount of energy per unit mass released from burning fossil fuels, in the first instance coal, solved this problem [3]. As a result, the production and consumption of energy increased drastically, and negative effect of human activities on nature started to depend on energy production processes, mainly because of the greenhouse gases emitted during the burning operation. In modern times, continuously increment of energy demand and given that fossil fuels are depletable compelled people to focus on environment friendly alternative energy sources one of the most promising of which is *solar energy*.

1.1 Solar Energy

All of the energy sources mentioned above are originated from fusion reactions occurred at sun which releases outcome nuclear energy in the form of electromagnetic wave. In spite of the tremendous amount of this energy reaching Earth's surface each day, unmediated consuming of this energy is limited with heating. Instead of directly converting solar energy to heat, transforming this energy to electricity provides opportunity of significant contribution to energy production and possibility to use this energy in various ways. This transformation process has been possible in last century correspondingly to developments in modern physics.

In 1839 the photovoltaic effect was first reported by Edmund Bequerel, who observed an electric current when light was sent towards a silver coated platinum electrode placed inside electrolyte [4]. In 1880s, first solar cell was constructed by Charles Fritts and finally first using of silicon p-n junctions took place in 1950s [4]. Since then, costs and efficiencies of solar cells have been increasing year by year. At Figure 1.1, increase in efficiencies of solar cells since 1975 can be seen [5].

The mechanism lying behind conversion of light energy to electric energy is explained by quantum mechanical phenomena named photoelectric effect. At the beginning of 20th century, one of the most confusing problem of physics was behavior of electrons that are spread from a material when it is exposed to light. Main discrepancy is that kinetic energy of electrons was found to be independent from intensity of light, but it changed with the frequency of light unlike the expectations of scientists. This led to the idea of light being made up discrete wave packets instead of its having a continuous structure and initiated quantum revolution. According to the quantum theoretical explanation of photoelectric effect, light packets, which were named photons, can pluck electrons from atoms in the case of photons having more energy than binding energy of electrons, and the energy difference transforms to kinetic energy of electrons.

By using semiconductor materials, this activity can produce electric current. When n-type and p-type semiconductors are combined, a structure named p-n-junction, which has great importance at modern electronic applications as well as solar cells, is formed. The uniqueness of this structure arises from distribution of electrons at interface of two types of semiconductors. Since n-type semiconductors have free electrons while p-type semiconductors have holes, at interfaces some free electrons move to p-type region and after the system reaches equilibrium, the charge distribution shown at Figure 1.2 is observed. This structure is a diode that allows current flow at only one direction, which means that if the voltage is applied in such a way that positive terminal is connected to p-type material while negative terminal is to n-type material (forward bias), current flow is possible, on the other hand for reverse connection (reverse bias), there will be no current. For photovoltaic devices, light takes on the task of voltage source. When light is sent to a p-n-junction, the equilibrium at interface of n-type and p-type materials is destabilized and this leads to the opportunity of obtaining energy in the event of connecting load to the system.

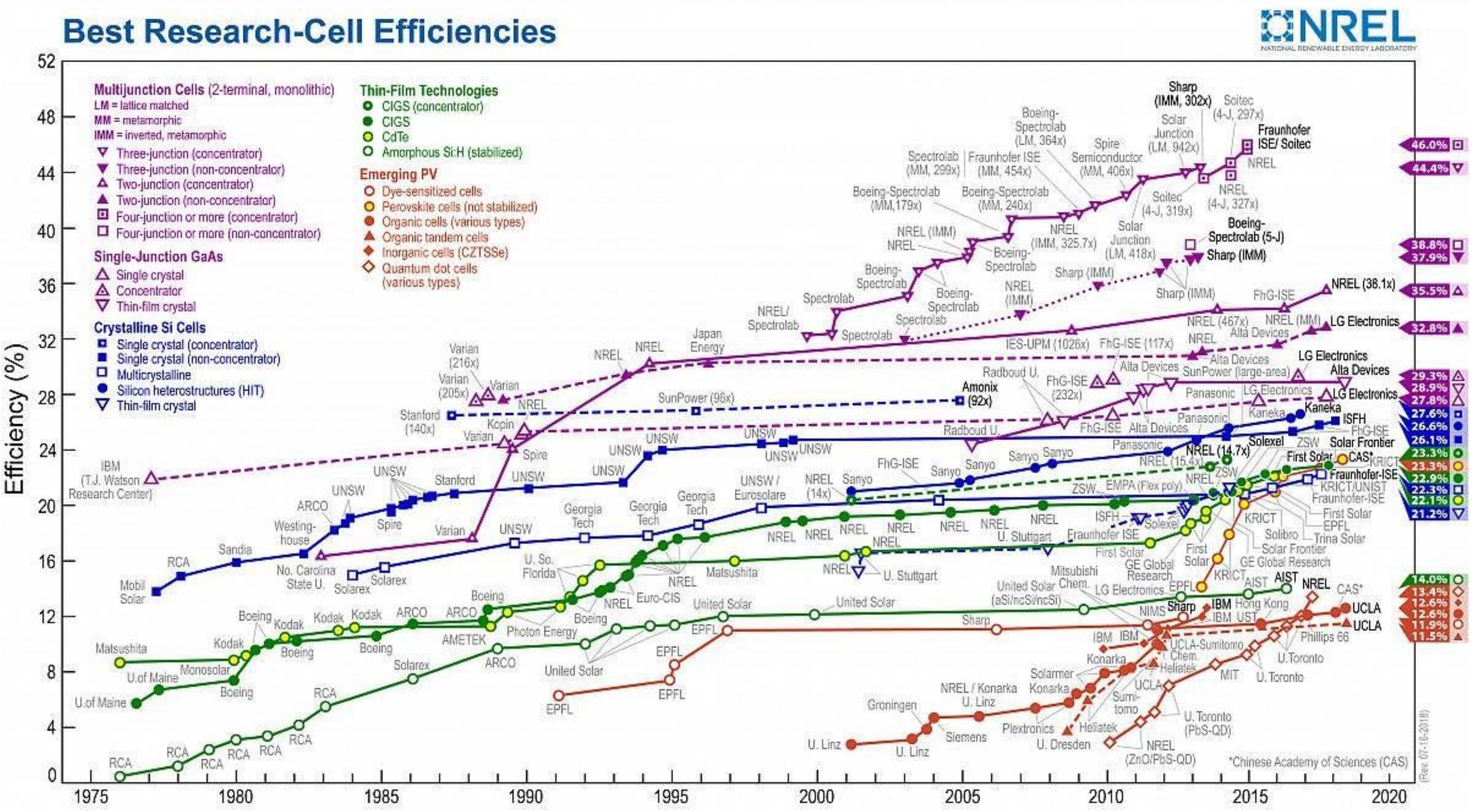

Figure 1.1. Increase in Solar Cell Efficiencies Year by Year [5].

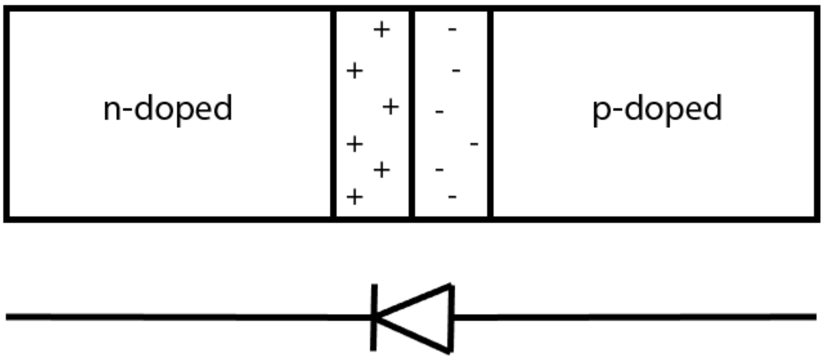

Figure 1.2. Charge Distribution at PN-Junction.

The effect of light is to provide energy for more electron to surpass the band gap. That’s why, relation between photovoltaic material and incoming light can be expressed as band gap structure of material as a function of wave vector. As shown at Figure 1.3, when graph of this function is drawn, two types of band gaps are distinguishable: direct and indirect band gaps. At former one, the momentum of resulting electron-hole pair becomes zero, while for latter one, there is a finite momentum and a phonon assistance is required for transition. As a result, absorption in indirect band gap materials is much weaker than that of in direct band gap semiconductors. This difference in efficiencies of absorption leads to the opportunity

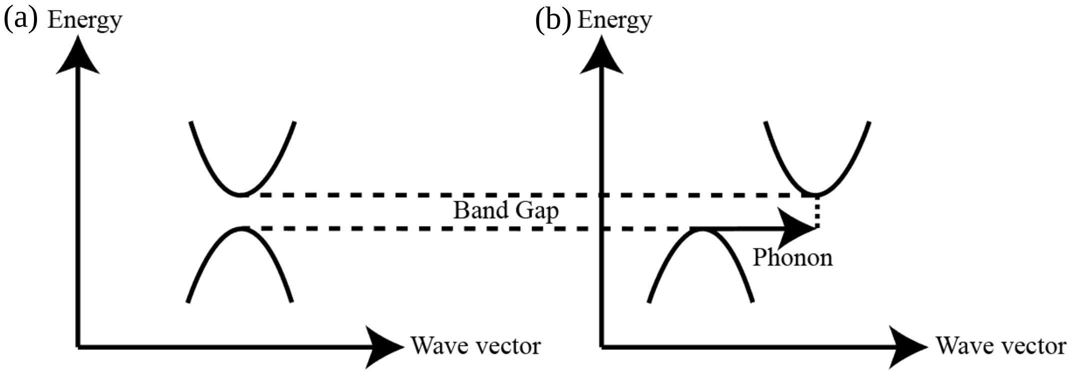

Figure 1.3. Two Types of Band Gaps: (a) Direct (b) Indirect.

of increase in overall solar cell efficiency by manipulating the photovoltaic materials chemically or metallurgically.

The enhancement of photovoltaic materials’ efficiency is extremely frequency-dependent. Because frequency of light adds up to same thing with its energy, efficiency of produced energy from interaction of photons with the electronic structure of photovoltaic materials relates to frequency of incoming light and its rapport with band gap of material. If the band gap is less than energy of photons, no current can be produced. If the gap energy is larger than that of photons, the amount of electric energy produced becomes equal to band gap and the excess energy transforms to heat. To sum up, both being more or less energetic of photons compared to band gap result in going down to drain of some incoming energy. This is the main limitation on enhancement of solar energy efficiency since solar light consists of a wide range of electromagnetic spectrum. This can be seen at Figure 1.4 where the solar irradiance at interface of space and Earth's atmosphere (red line: ASTM / E-490), at sea level (black line: ASTM / G173-03) and measured at imperfect conditions (green line) are shown [6]. The large bandwidth of solar light can be clearly seen in Figure 1.4. It is crucial to take advantage of the wide bandwidth in order to increase efficiency of energy harvesting.

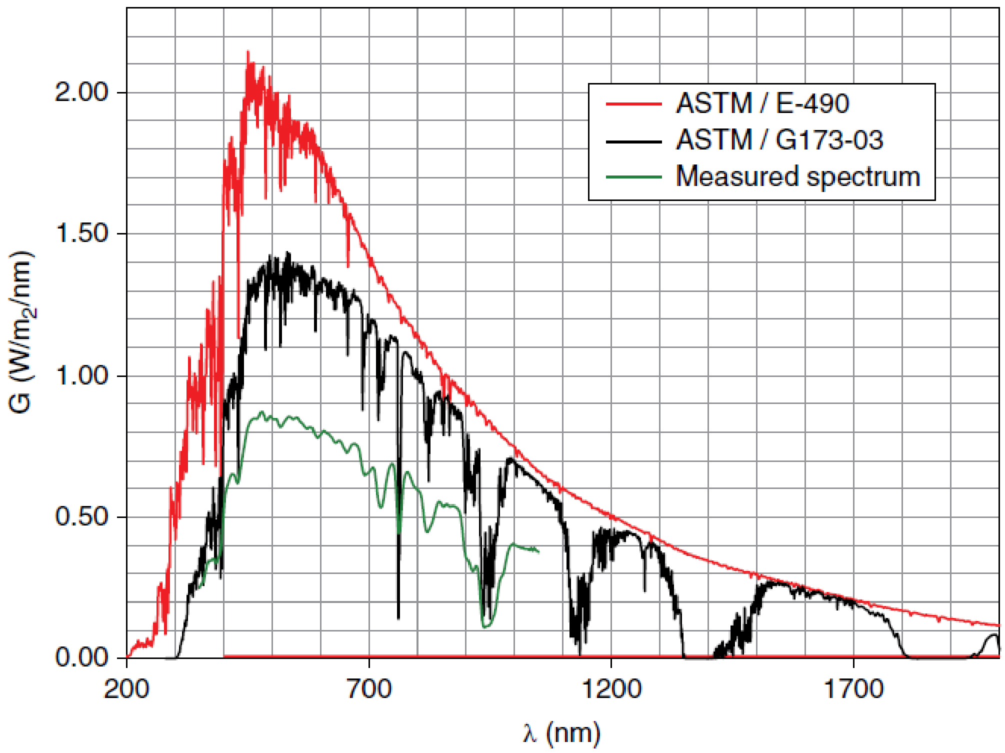

Figure 1.4. Solar spectra: ASTM E-490 representing AM0 (black line), ASTM G173-03 representing AM1.5 (red line), and a measured spectrum (green line) showing the differences that can occur in reality. Data from ASTM and University of Twente, The Netherlands. Courtesy of A. Reinders, University of Twente (Adapted from [6]).

1.2 Spectral Splitting

Several materials can be used inside a solar cell in order to increase energy output from solar cells. Multi-junction solar cells, are built for this purpose. These solar cells consist of several layers with materials that have different electronic band structures. In these solar cell constructions, the highest energy photons are absorbed by the top layer and subsequent layers absorb lower energy photons. Such applications results in significant increase of solar cells efficiency from early nineties to today [7]. However, there are several disadvantages of this technique: i) The energy losses due to reflection at interfaces of mechanically stacked devices and ii) the complexity of fabrication via epitaxial growth process. On the other hand, fabrication of laterally displaced junctions is simpler and these junctions provide similar efficiency as the vertically stacked junctions. The drawback of this procedure is that laterally displaced junctions require the incident white light to be spectrally split. Here, effective spectral splitting is a challenge for broadband solar light.

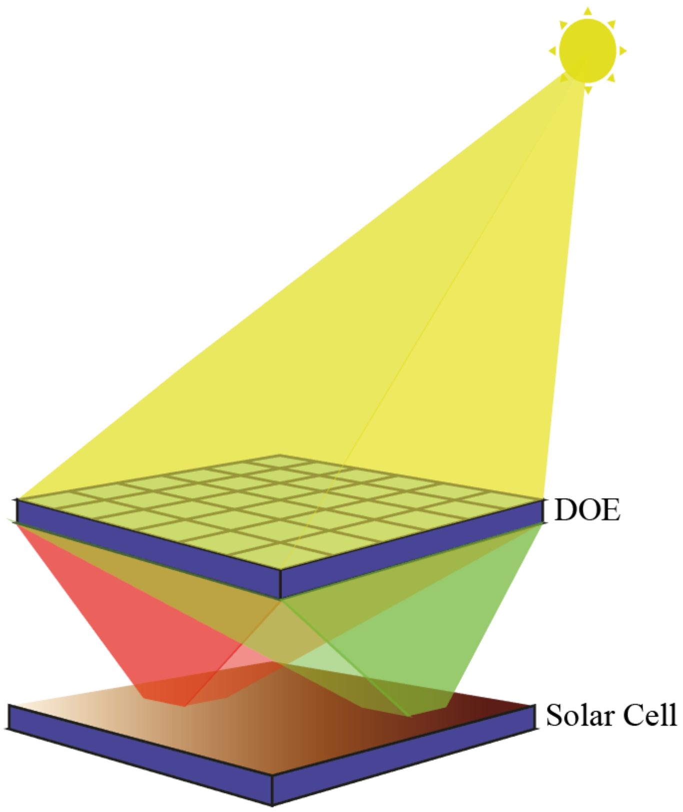

Figure 1.5. Illustration of Spectral Splitting.

In Figure 1.5, splitting of incoming light is demonstrated. The upper structure in the figure is an optical element that achieve spectral splitting while the bottom structure represents photovoltaic material where the electric current is produced. Introducing a convenient optical element is as important as using appropriate photovoltaic materials for high efficiency. Diffractive optical elements which enable micro or nanoscale control of light provide better precision on controlling light and have advantageous over other optical elements as lenses.

Diffractive optical elements (DOEs) have been widely investigated and employed in several applications in recent years. Many applications in photonics started to employ DOE which control diffraction of light. Multi-beam processing, imaging and spectroscopy can be listed as fields that have recently taken the advantageous of DOF structures [9–11]. Study of Kim et al. merits to be mentioned as an example of flexibility and opportunity provided by DOEs [8]. In this study, which demonstrate a design of DOE that works at broadband frequencies gives the desired outputs with high splitting efficiency. As can be seen in Figure 1.6, two planes that are DOE plane and image plane are aligned in order to produce the output patterns that are shown Figure 1.7. Single DOE structure is designed for this purpose and its structure becomes as shown in Figure 1.8-a, each pixels of which represents height of that point and these height differences are the way to manipulate incoming light, which will be explained in detail in Theory part. In Figure 1.8-b, the high resolution view of the profile can be seen. The results which are similar to Figure 1.7 are also shown at Figure 1.9-a, b and c.

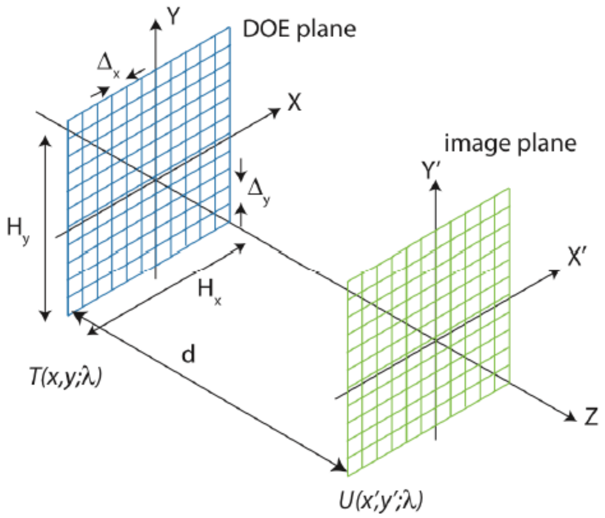

Figure 1.6. Schematic of the optimization problem geometry.(Adapted from [8]).

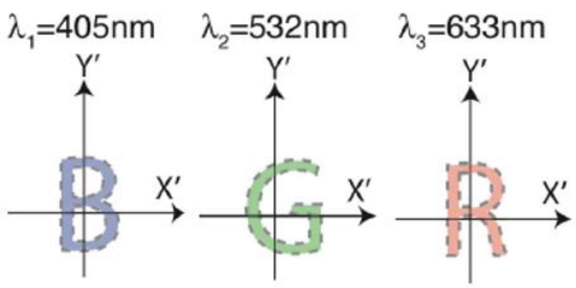

Figure 1.7. Target binary images used for the design example containing 3 letters to be reconstructed by 3 distinct wavelengths (Adapted from [8]).

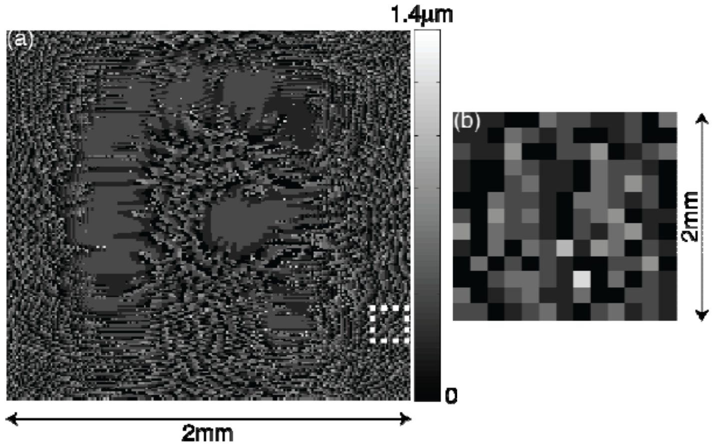

Figure 1.8. Multi-wavelength DOE designed for 3 discrete wavelengths and target images. (a) DOE's optimized height profile map. (b) Magnified view of a 13 X 13 pixels region outlined by the white square in (a). (Adapted from [8]).

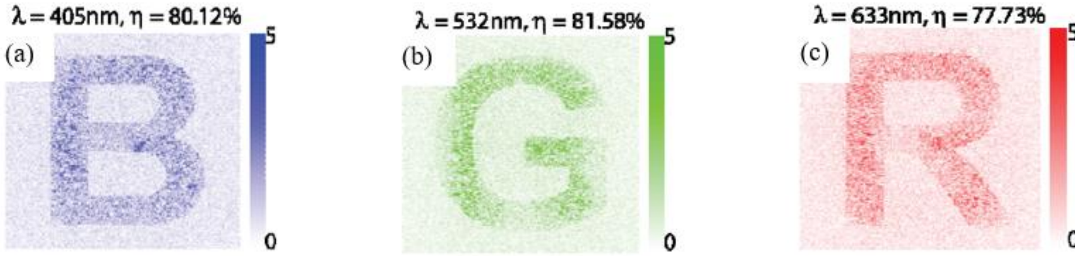

Figure 1.9. Reconstructed image amplitude distributions at (a) λ = 405nm, (b) 532nm and (c) 633nm (Adapted from [8]).

The method developed for color holography can be adopted to spectral splitting of sunlight and concentrate to a desired region. The only thing remains is to engineer diffractive optical element expediently. Since it is more fundamental, splitting light into colors dates back to relatively early times, beginning of the 1990s. In 1993, a 64×64 array of binary micro-optical structures was used for splitting light into three colors by Farn et al. [12]. In 1996, Dong et al. created a non-binary diffractive phase element (DPE), which is calculated iteratively [13]. As can be seen at Figure 1.10, the results of this study are quite promising that concentrate three wavelengths at three distinguishable regions. Here λ_1, λ_2, and λ_3 are 514.5 nm, 590 nm and 632.8 nm respectively. However, this kind of splitting is not useful for solar applications since it works at too narrow range of wavelength. On the other hand, at the work of Kim et al., the process is applicable to almost whole range of sunlight spectrum, from 350 nm

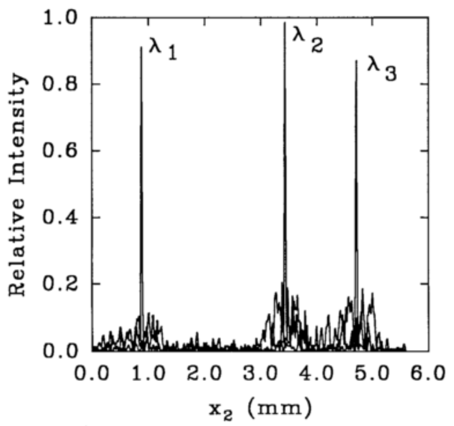

Figure 1.10. Output intensity distribution generated by the designed DPE (Adapted from [13]).

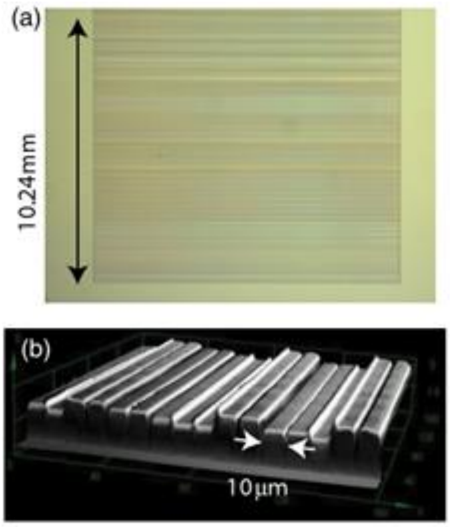

Figure 1.11. (a) Bright-field image of a polychromat. (b) Magnified optical profilograph of a section of the polychromat. (Adapted from [14])

to 1100 nm [14]. In the study, this broadband sunlight is aimed to be split into two range of wavelengths, one is between 350-800 while the other is between 801-1100, and each of them sent to corresponding regions. The structure is provided in Figure 1.11 and is used to obtain outputs that are given in Figure 1.12. In addition, focusing efficiencies for all wavelengths for two cases are also shown at Figure 1.12-c and d respectively. The spectrally averaged optical efficiency is found to be 70%, which means that totally 70% of light is collected to desired regions accordingly to its wavelength. This study also demonstrates the effect of spectral splitting on solar cell's power efficiency by performing electrical characterization. The characterization that is realized for both pair of copper indium gallium selenide (with band gaps of 1.05 and 1.5 eV) and silicon/gallium arsenide (Si/GaAs) cells ends up with decreasing of energy produced by low band gap material, which, however compensates by the increment at output energy from high band gap material. As a result, total output power density increases ~42% for copper indium gallium selenide cells and ~22% for Si/GaAs cells, with respect to the case of no spectral splitting performs [14]. Instead of two, splitting light into three ranges of frequency yields to even more increase in efficiency. For example, in the study of Mohammad et al., the increase is stated to be 35.52% [15]. Note that in this study, gallium indium phosphide (GaInP), gallium arsenide (GaAs) and silicon (Si) are used as photovoltaic materials, so the increase in efficiency should be compared to that of Si/GaAs cells mentioned before and it can be said to be 13.52% more than the previous case.

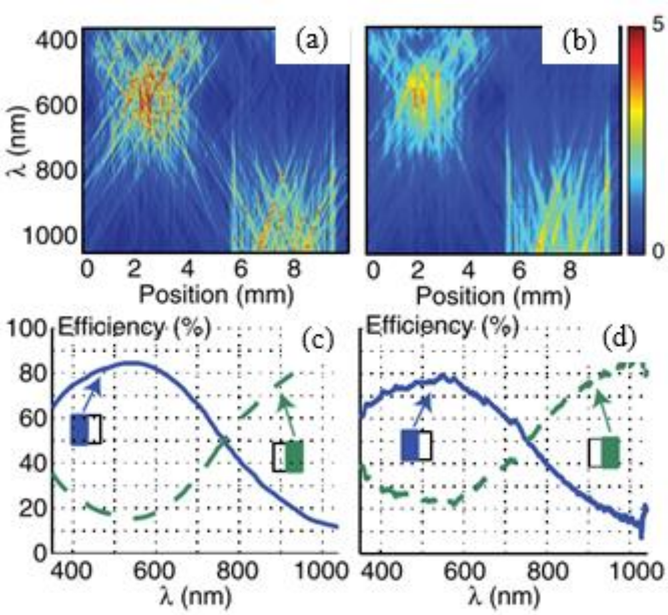

Figure 1.12. Spatial-spectral map at the polychromat reconstruction plane: (a) simulated and (b) measured. Optical efficiency of the polychromat as a function of wavelength: (c) simulated and (d) measured. The solid and dashed curves represent light diverted to the high- and low- band-gap cells, respectively (Adapted from [14])

These results are quite promising and paves the way for even more enhancements for solar cells. However, for both cases manipulation of structure that splits light is restricted to one dimension. Ability of creating structures with two dimensional control provides much more flexibility, and also more effective splitting. Not only the structure but also the alignment of photovoltaic cells can be arranged two dimensionally. For example, dividing a square into four and displacing four different materials to these sub-squares, or even calculating optimum solar cell localization in addition to pattern of optical structure becomes possible and provides opportunity of manipulating the system in many different ways. In next chapter, the theory of spectral splitting with mathematical formulation is explained and our algorithm for calculating the optimized DOF is introduced.

CHAPTER 2

THEORY

The nature of light has been one of the most contradictive issue throughout the history of science. Its demonstrating both particle and wave characteristics has created confession among scientists. However, today the problem seems to have been solved by considering the quantum nature of light, which gives a complete description of both behaviors. Since we use diffraction for spectrally splitting sun light, we don't need to expand on the quantum theory and it is adequate to assume light to be wave, which is described mathematically as:

$$\nabla^2 u(\boldsymbol{r}, t) - \frac{1}{v^2}\frac{\partial^2 u(\boldsymbol{r}, t)}{\partial t^2} = 0, \qquad \text{Eq.2.1}$$

where v is the reduced speed of light waves and $\mathrm{u}(\mathbf{r}, \mathrm{t})$ the wavefunction that depends on position $\mathbf{r} = (\mathrm{x}, \mathrm{y}, \mathrm{z})$ and time t. Since the equation is linear, sum up of any two wavefunctions that are solutions of it, is also a solution. This is a unique property of waves and known as superposition principle. As a more physical description, this principle states that the resulting wave amplitude at a point is given by the algebraic sum of all constituent wave amplitudes at that location. This behavior leads to interference.

Interference can be observed when two or more waves encounter at a position, where they superimpose and create distinct pattern. The pattern is composed of high intensity regions, where the waves constructively interfere, and low intensity regions, where the waves destructively interfere. By manipulating relative phases of light beams, several interference patterns can be created and this provides a useful tool for several photonic applications.

Another wave property of light is diffraction, which is bending and diverging of light when it encounters tiny obstacles or slits sizes of which are comparable to wavelength of light. This phenomenon is explained with the help of Huygens-Fresnel Principle, which states that each points on a wavefront can be thought as a source of spherical wavelet and the interference of these wavelets determines the structure of wave at any subsequent time. Depending on the distance, Fresnel diffraction for near-field or Fraunhofer diffraction for far-field is obtained. For deciding whether Fresnel approximation or Frounhofer approximation should be used, the Fresnel number must be calculated according to the equation:

$$\mathrm{F} = \frac{\mathrm{a}^2}{\mathrm{L} \cdot \lambda} \qquad \text{Eq.2.2}$$

where a is characteristic size of the aperture, L is the distance between screen and aperture and λ is wavelength of light. If this number is much smaller than 1, it means that we are in Frounhofer regime. In our study, this condition is fulfilled so we consider Frounhofer approximation.

For a plane wave sent towards a single slit as can be seen in Figure 2.1, if all points at permeant part of the structure is assumed to be spherical wave sources, then effect of each of these sources at a point P can be written as:

$$dU_P = \left(\frac{U_L ds}{r}\right) e^{i(kr - \omega t)}, \qquad \text{Eq.2.3}$$

where dU_P is the differential wave amplitude at point P, U_L the wave amplitude per unit width of slit at unit distance away, r the distance between the interval ds and the point P, k and ω the wave parameters which are wavenumber and angular frequency respectively. The distance r can be expressed as $r = r_0 + \Delta$, where r_0 is the distance from midpoint of slit to P, and Δ is the path difference which is equal to product of vertical distance from optical axis, s, and sinus of the angle α. So Eq. 2.3 evolves to:

$$dU_P = \left(\frac{U_L ds}{r_0 + s.sin\alpha}\right) e^{i(k(r_0 + s.sin\alpha) - \omega t)}, \qquad \text{Eq.2.4}$$

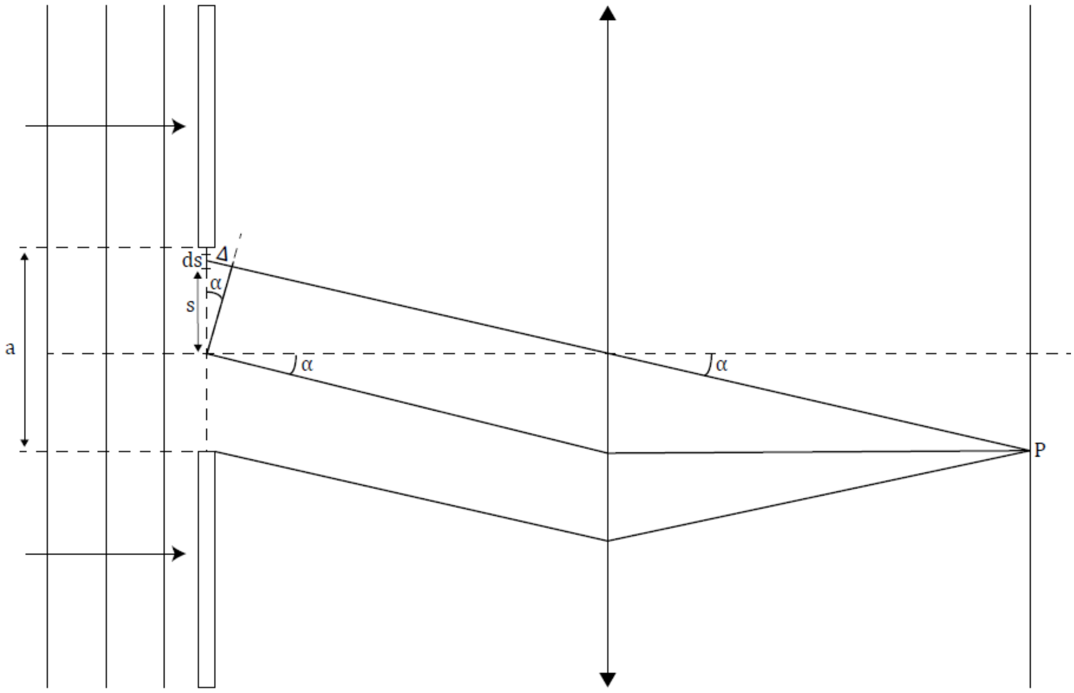

Figure 2.1. Diffraction from a single slit.

Since $s.sin\alpha$ is very small compared to r_0, it can be neglected at denominator of amplitude, however, it should be taken into account at phase because of phase's being very sensitive to small changes. After arranging the terms, the equation yields to:

$$dU_P = \left(\frac{U_L ds}{r_0}\right) e^{i(kr_0 - \omega t)} e^{ikssin\alpha}. \qquad \text{Eq.2.5}$$

Integrating over the slit which is positioned between $-a/2$ and $a/2$ gives us:

$$U_P = \frac{U_L}{r_0}\frac{1}{iksin\alpha}\left[e^{(ikasin\alpha)/2} - e^{-(ikasin\alpha)/2}\right]e^{i(kr_0 - \omega t)}. \qquad \text{Eq.2.6}$$

If Euler's formula is applied, the equation becomes:

$$U_P = \frac{U_L a}{r_0}\frac{sin\theta}{\theta}e^{i(kr_0 - \omega t)}, \qquad \text{Eq.2.7}$$

where $\theta = (kasin\alpha)/2$. The intensity of this resultant wave is proportional to square of wave amplitude and it is in the form of:

$$I = I_0 \frac{sin^2\theta}{\theta^2}, \qquad \text{Eq.2.8}$$

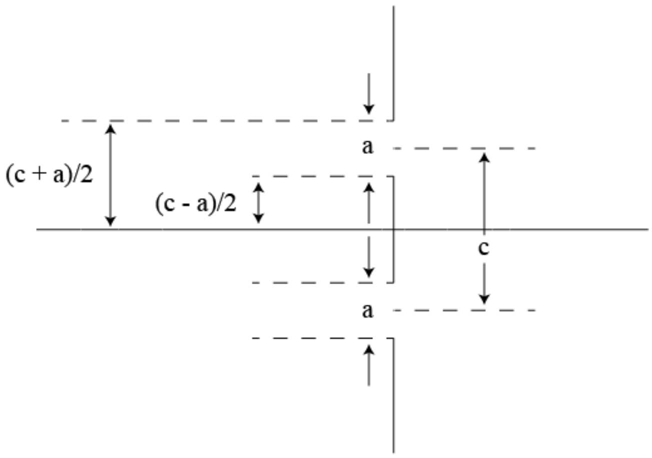

Figure 2.2. Sheme of double slit diffraction.

where I_0 is a constant term which is related to the value of $\left(\frac{U_L a}{r_0}\right)^2$. Here, intensity is highest at center and lower intensity peaks align symmetrically such a way that peak intensity decreases as long as distance from the center increases. This result provides us the opportunity of deriving an equation for intensity pattern of a two dimensional rectangular aperture with edge sizes of a and b, by adding a term to Eq. 2.8 for extra dimension. This leads to the equation:

$$I = I_0 \frac{sin^2\theta sin^2\varphi}{\theta^2\varphi^2}, \qquad \text{Eq.2.9}$$

where $\theta = (kasin\alpha)/2$ and $\varphi = (kbsin\beta)/2$. Here α and β are the angles between line connecting center of aperture and interested point on screen, and two vertical axis.

For the case of two slits, as can be seen at Figure 2.2, integration of Eq. 2.5 should be made for both slits independently and sum of them should be used for intensity calculation. The interval of integration limits are from $(c-a)/2$ to $(c+a)/2$ for upper slit and from $-(c+a)/2$ to $-(c-a)/2$ for lower slit. Sum of the results for these two interval becomes:

$$U_P = \frac{U_L}{r_0}\frac{1}{iksin\alpha}\left[e^{(ik(-c+a)sin\alpha)/2} - e^{(ik(-c-a)sin\alpha)/2} + e^{(ik(c+a)sin\alpha)/2} - e^{(ik(c-a)sin\alpha)/2}\right]e^{i(kr_0 - \omega t)}. \qquad \text{Eq.2.10}$$

Applying Euler's formula to the equation yields to

$$U_P = \frac{U_L}{r_0}\frac{2asin\theta}{\theta}\cos(\gamma)\, e^{i(kr_0 - \omega t)}, \qquad \text{Eq.2.11}$$

where $\theta = (kasin\alpha)/2$ and $\gamma = (kcsin\alpha)/2$. Finally, the intensity pattern of this field becomes:

$$I = 4I_0\frac{sin^2\theta}{\theta^2}cos^2\gamma. \qquad \text{Eq.2.12}$$

As can be seen from Eq. 2.8, 2.9 and 2.12, the intensity pattern depends on the wavenumber of initial wave, distance between slit and screen, width and displacements of the slits. For creating a desired pattern at a fixed screen position, the variables that can be modified are wavenumber of wave and the slit width. A way of creating desired intensity pattern on the screen is to use more than one slit with different positions and widths, however variety of possible patterns is limited for this

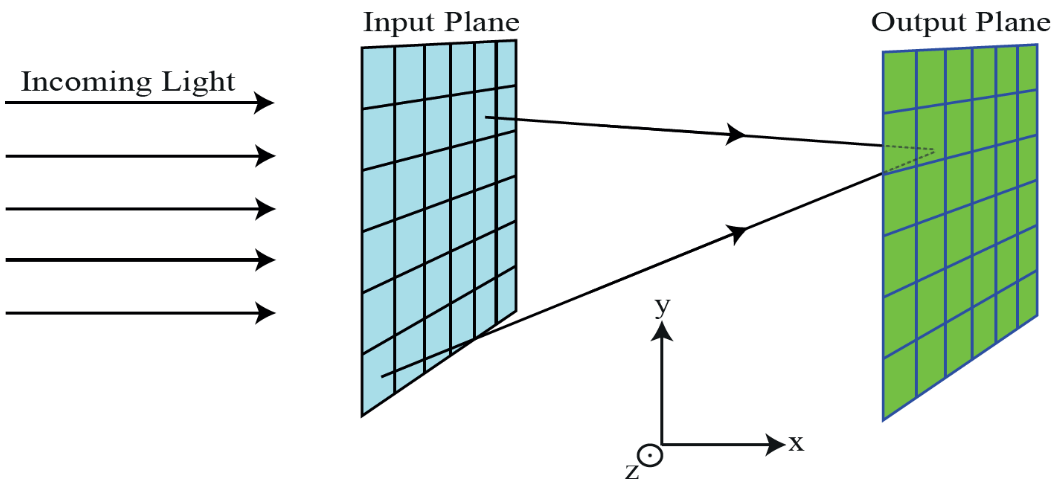

Figure 2.3. Alignment of input and output planes which are divided into pixels.

case. On the other hand, directly manipulating light provides much more degree of freedom.

Instead of single slit, taking advantage of multiple slits makes it possible to manipulate several diffracted light beams independently, provides necessary degrees of freedom for spatial control of light. By changing the phases of beams, the resultant pattern can be structured. Figure 2.3 shows an alignment at which the output plane where the pattern will be created is also divided into squares (pixels) because it is necessary for computationally calculating an input effect on output. All calculations of our study are based on the relation between input and output pixels. A plane wave is assumed to be sent to input plane and after its propagation by a distance at x direction, an intensity pattern is observed at output plane. The change is determined by considering the phase difference required for each input pixels to obtain desired intensity distribution at the target plane. To clear up, input plane can be represented by a matrix each element of which is connected to output plane via the optical path length at the corresponding position.

By calculating phase delays for each pixel, structure of wave just after the input plane is obtained, however at output plane the wave will have totally different structure. Here, each input pixel can be thought as a source of spherical wavelets with different phases and evolution of intensity pattern with distance can be calculated by interfering these wavelets. In Figure 2.4, the process of light diffracting at input pixels and create patterns at output plane is shown. In Figure 2.4 (b), the waves interfere with each other randomly, while in Figure 2.4 (c), they interfere constructively at center of the figure. Corresponding phasor representations are also shown next to the figures.

Given the perpendicular distance of two plane, phase of a wavelet diffracted from a specific input pixel, on a specific output pixel can be calculated. The resultant value of wave function at an output pixel is sum of the effects of all input pixels on this output pixel and calculated according to the following equation:

$$U_{2m} = \sum_{k=1}^{N} G_{mk} U_{1k} \qquad \text{Eq.2.13}$$

where U_{2m} is the value of wave function at mth pixel of output plane, U_{1k} the value of wave function at kth pixel of input plane, G_{mk} the kernel function that fulfil the relation between kth pixel of input and mth pixel of output wave functions, and N the total number of pixels which is same for input and output planes. Eq. 2.13 indicates that the effect of an input pixel on an output pixel is determined by two values; U_1, which contains the information of phase just after the input plane and G, which includes the information of distance between input and output pixels.

The value of U_{1k} is determined by the product of amplitude with exponential form of optical path length, as represented below:

$$U_{1k}(\lambda) = \rho_{1k} \exp[i2\pi h_{1k}(n_S - 1) / \lambda], \qquad \text{Eq.2.14}$$

where ρ_{1k} is the amplitude and h_{1k} the depth value of kth input pixel; n_S is the refractive index of input material and λ is the wavelength of light. Optical path length

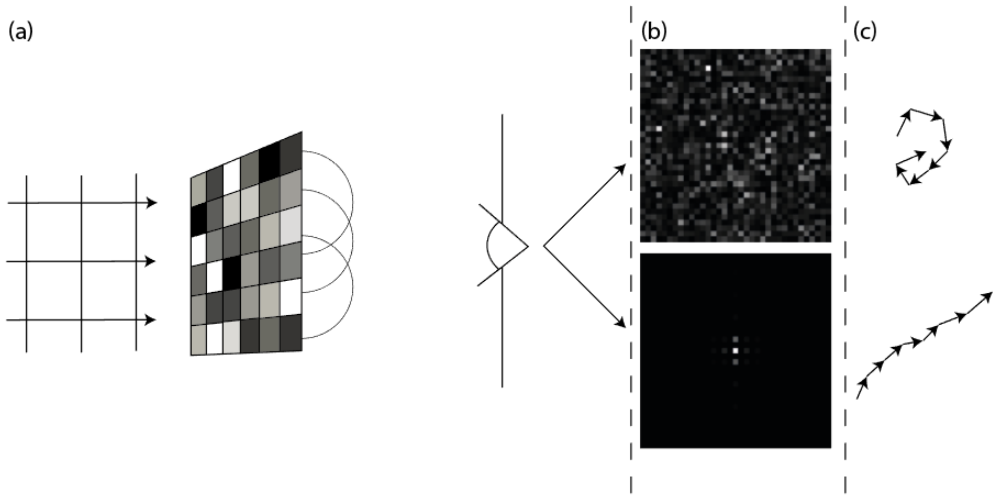

Figure 2.4. a) Experiment setup, b) two possible outcomes c) their phasor representations.

is indicated by the value $h_{1k}(n_S - 1)$, which specifies how much phase delay does light gain due to the distance it propagates inside the high index medium. Since the more it experiences high index media, the less it propagates through air, total optical path length becomes subtraction of that would occur if there was air instead of high index medium, from the optical path length of high index media.

The parameter G_{mk}, introduced in Eq. 2.13 has the following form:

$$G(y_2, y_1; l, \lambda) = \left(\frac{1}{i\lambda l}\right)^{1/2} \exp(i2\pi l/\lambda) \times \exp(i\pi(y_2 - y_1)^2/\lambda l), \qquad \text{Eq.2.15}$$

where l is the distance between input and output planes, y_1 and y_2 are the positions of input and output pixels respectively. This equation is useful for 1-dimensional geometries, however for 2-dimensional geometries that is shown in Figure 2.3, the equation evolves to:

$$\begin{aligned} G\big(y_2, y_1, z_2, z_1\, ; l, \lambda\big) \\ &= \left(\frac{1}{i\lambda l}\right)^{1/2} \exp(i2\pi l \,/\, \lambda) \\ &\times \exp(i\pi((y_2 - y_1)^2 + (z_2 - z_1)^2) \,/\, \lambda l), \end{aligned} \qquad \text{Eq.2.16}$$

where z_1 and z_2 are the second position components of input and output pixels respectively. The phase difference denoted in these equations is result of locations of input and output pixels at yz-plane. The effect of distance between planes doesn't change pixel by pixel since two planes are parallel. So for a specific value of l and single wavelength λ, G value of two pixels only depends on their position differences at yz-plane.

To find a complete intensity distribution at output plane, U_2 should be calculated for all output pixels and the intensity should be calculated pixel by pixel, according to the following equation:

$$I(y_2, z_2;\ \lambda) = \left|\sum_{k=1}^{N} G(y_2, y_1, z_2, z_1\, ; l, \lambda) \cdot U_{1k}(\lambda)\right|^2. \qquad \text{Eq.2.17}$$

By using equation above for all output pixels, complete intensity pattern at output plane for a specific optical path length pattern at input plane can be obtained. However, it is more complicated to find out the optical path length pattern that will result in a desired intensity pattern at output plane. With the help of iterative algorithms, it is possible to change input pattern and calculate the output pattern several times. By comparing the results, the input pattern that gives the output pattern best fit to desired intensity pattern can be selected. If the purpose is to obtain different intensity patterns for different wavelengths of light by using a single input pattern, then for each wavelength and corresponding intensity pattern the calculations should be made independently and the best fit for all of wavelengths should be selected.

In Figure 2.5, the algorithm and calculations are shown schematically. Left side of the figure demonstrates the main algorithm where two calculations for different patterns are made and the one gives better result is assigned to a variable that will be used in next iteration. The right panel of the figure, the summary of calculation process, which is explained in detail above, can be seen.

Since the operation is wavelength dependent, it provides all the tools for focusing different colors to different regions. By choosing the output pixels to which specific wavelengths of light will be focused, and comparing intensity changes of these positions for each frequencies during the process, the input profile corresponding to highest intensities at desired points is selected. For focusing light to a group of pixels, the comparison can be made between sum of intensities of pixels in the group, and the input pattern that gives highest sum is chosen.

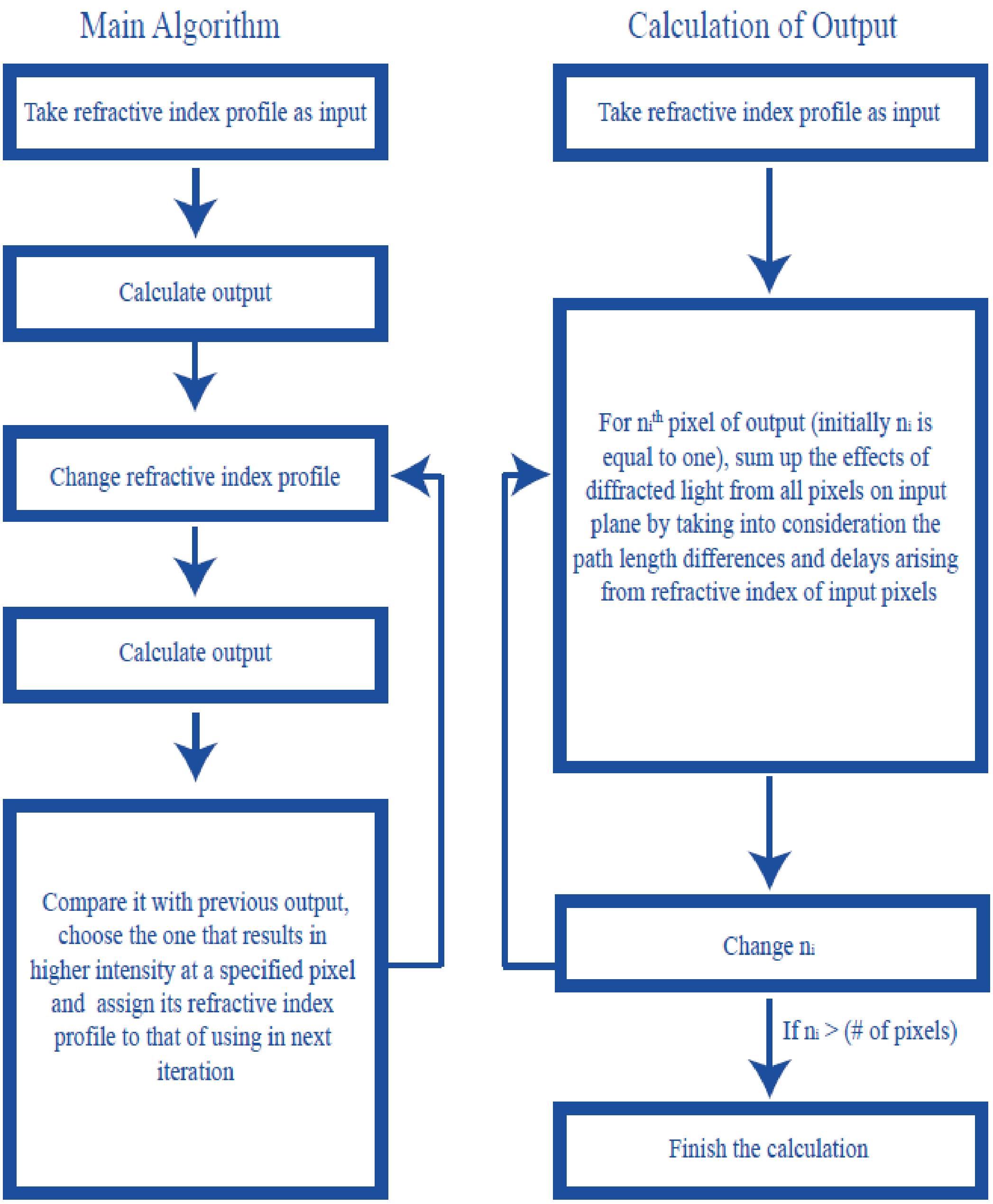

Figure 2.5. Scheme of algorithm.

CHAPTER 3

RESULTS

3.1 Concentrating Light Using Fresnel Zone Plates

A zone plate consists of several radially symmetric rings called zones, which can be either opaque or transparent (Figure 3.1). First calculation we made is for Fresnel Zone Plate, which is an optical element that controls interference of light, and generally used for focusing of light at a given wavelength. Its main working principle is to collect light in a small region by selectively controlling the transmitted light that pass though concentrated rings. The interference pattern at the target position can be modified via selectively blocking or allowing the transmission through the rings that are multiples of the wavelength. The thicknesses of zones are adjusted so that light transmitted by the transparent zones constructively interferes at the desired focus. For deriving radii of zones (r), distance from center of plate to desired focus (f), and distance from any source point on the plate to focus (l) should be considered, as illustrated in Figure 3.1. A basic relation between these variables is given by:

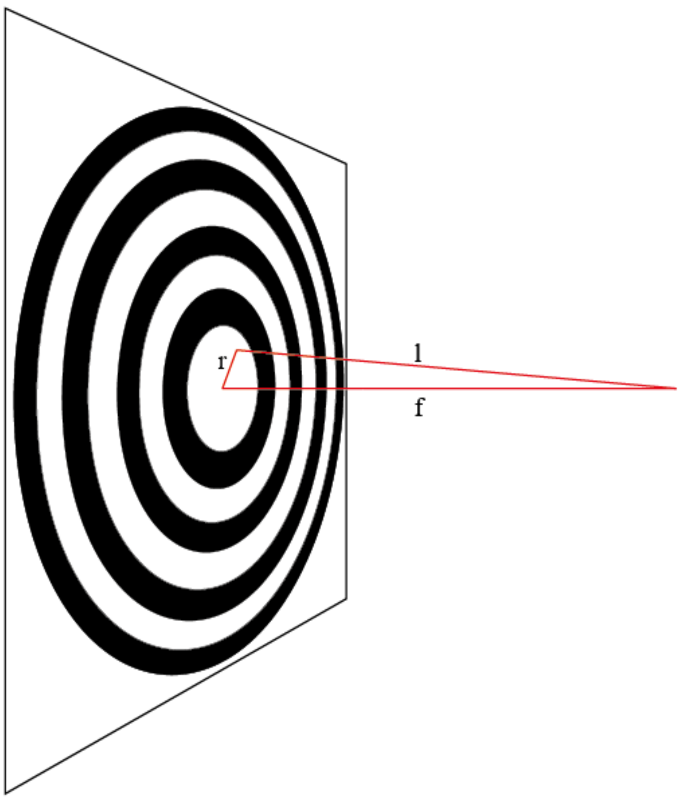

Figure 3.1. Shematic illustration of Fresnel zone plate.

$$l = \sqrt{r^2 + f^2}. \qquad \text{Eq.3.1}$$

For constructive interference at the focus position, l must differ by no more than $\lambda/2$ from f. By generalizing this for all zones, the following formula can be obtained:

$$\frac{(m-1)\lambda}{2} < l - f < \frac{m\lambda}{2}, \qquad \text{Eq.3.2}$$

where m is the positive integer from 1 to total number of zones. To find radii of zones, the difference $(l - f)$ considered to be equal to $m\lambda/2$ and the following formula is obtained:

$$r_m^2 = m\lambda\left(f + \frac{m\lambda}{4}\right). \qquad \text{Eq.3.3}$$

This equation indicates radii of all opaque and transparent zones of plate.

The zone plate can also be in a continuous structure. In this case, the opacity of a pixel can be given by:

$$\frac{1 \pm \cos(akr^2)}{2}, \qquad \text{Eq.3.4}$$

where a is a scaling factor that determines number of pixels, r is the distance from the center of plate to pixel and k is the wavenumber.

We analyze both binary and continuous zone plates. For binary zones, our algorithm first calculates all radii and creates a vector from these values. Then for all specific pixels, it subtracts the vector from the distance of the central pixel of the plate. Since the elements of radii vector are sorted ascendingly, the index of first negative element of resultant vector gives the index of smallest radius that comprises the specific pixel. Moreover, if the index is even, the pixel belongs to transparent region, otherwise it belongs to opaque region. Note that first element of radii vector is 0. Ultimately, all pixels that belong to transparent regions are set 1, others are set 0. An example is shown in Figure 3.2-a where 40 plates are placed inside an area of $0.00475 \times 0.00475 \text{ m}^2$ square.

a) b)

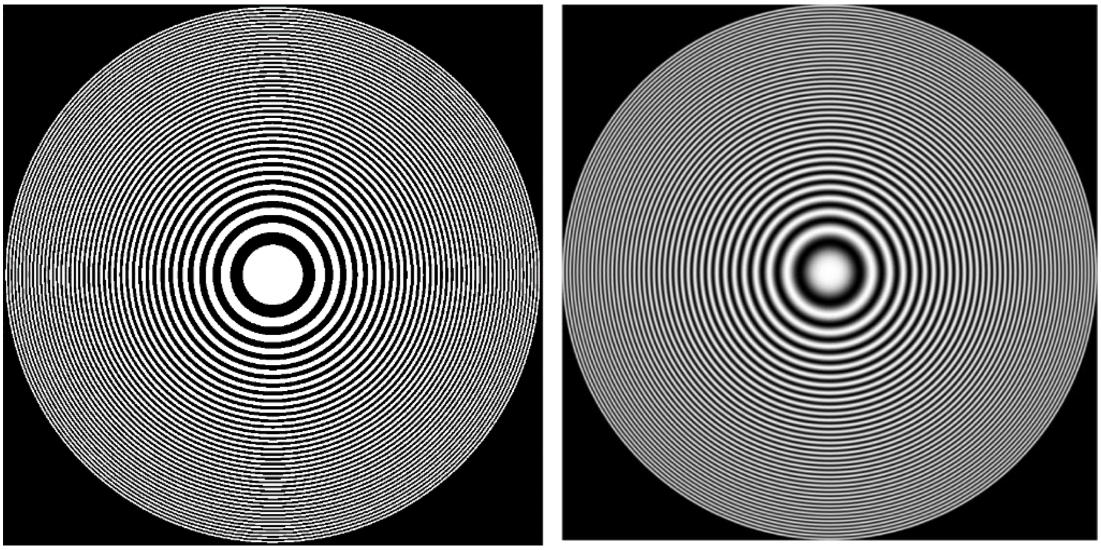

Figure 3.2. a) Binary Fresnel zone plate. b) Continuous zone plate. Both are comprised of 40 plates inside an area of $0.00475 \times 0.00475\ m^2$.

For continuous zone plate a different algorithm is used. Because the formula needs to have a constant term inside the cosine for scaling the function in accordance with the given number of plates, a linear learning method is used. We observe that this method is effective enough for our purpose. The linear learning algorithm is based on first creating a random number and assign it as a product "a" inside cosine. Then by comparing the number of plates to the desired value, the randomly produced number is increased or decreased. This process is repeated until the desired number of zones is obtained. If too much trials are made but the desired number of zones can't be reached, then we add a small number to the variable and repeat the process until the target is reached. Lastly, we operate the function using the constant term that we found in previous step, and construct the plate. As an example of continuous Fresnel zone plate, a structure with 40 plates can be seen in Figure 3.2-b. We design zone plates that concentrate light at f = 0.1 m away from the plate. The intensity distribution of light passing through the zone plate is calculated by taking the Fourier transform of the designed plate [16]. The intensity pattern shown in Figure 3.3 with also its magnified image, is normalized with respect to the incoming light. Cross-section of this

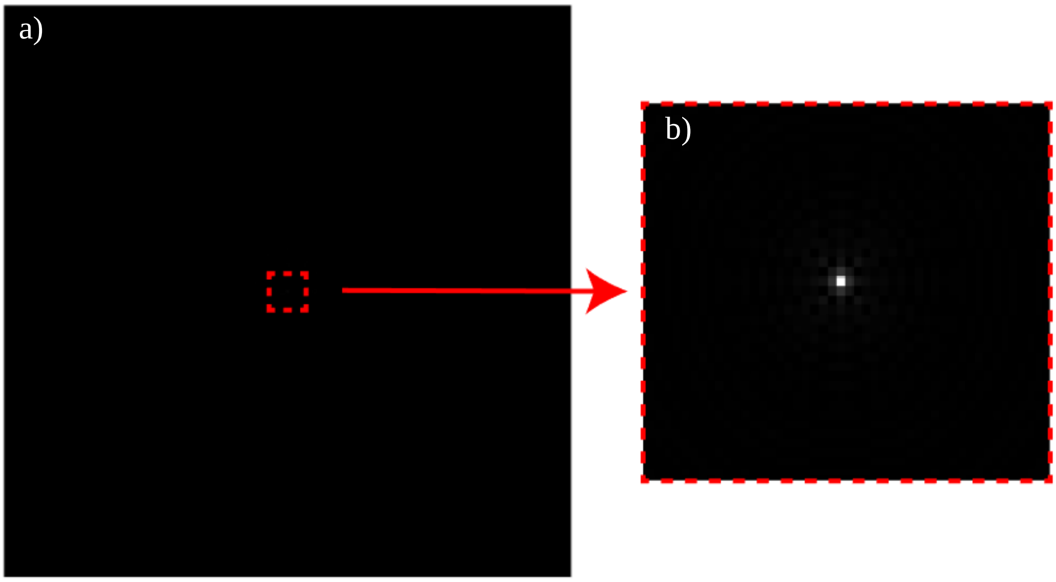

Figure 3.3. Resultant intensity pattern of zone plates for 40 plates inside an area of 0.00475×0.00475 m^2. a) Complete result. b) Magnified result.

normalized intensity distribution is shown in Figure 3.4 for both binary and continuous plates. The accumulation of intensity at center is clear for both cases, however the peak at continuous case is 1% higher than that of binary case because of more light being able to pass through the plate.

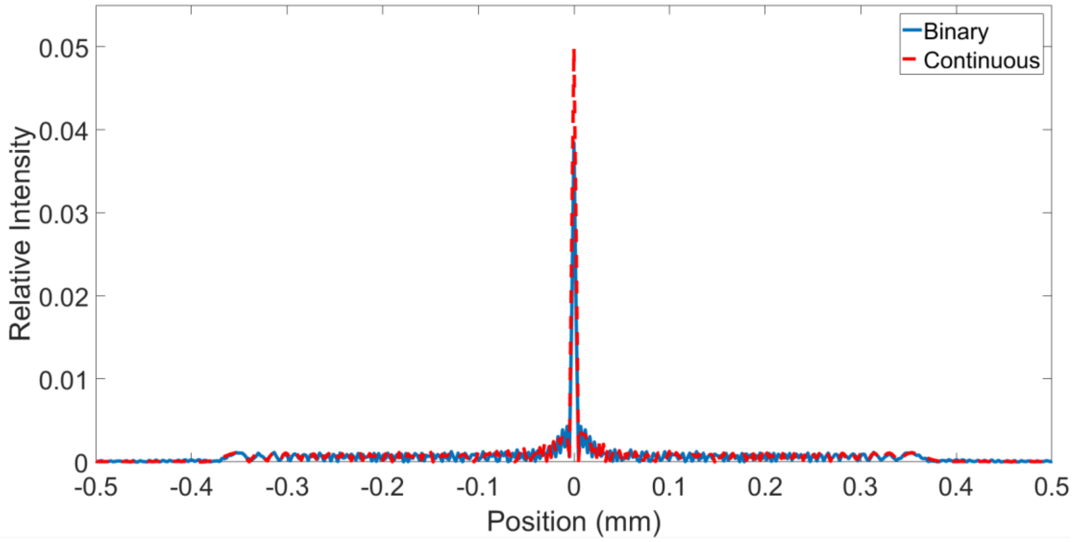

Figure 3.4. Relative intensity versus position for binary and continous zone plates with 40 plates inside an area of 0.00475×0.00475 m^2.

3.2 Concentration of Light via 1D Diffractive Optical Elements

Instead of blocking some of the incoming light for providing constructive interference at a desired point, it is more effective to allow all the light passing through with variations of phase, which also enables manipulating output intensity pattern as mentioned in the Theory part. Structures used for creating spatial phase variations are called diffractive optical elements and our calculation is performed for a 1-dimensional diffractive optical element which is optimized to focus a single frequency. Figure 3.5 and Figure 3.6 show the optical path length pattern and corresponding intensity distribution respectively. The intensity distribution is calculated for 400 nm light sending towards diffractive optical structure with 1 cm length and 10 µm depth. The structure is divided into 1000 pixels with a pixel size of 10 µm. Note that distance from the diffractive optical element to output plane is 40 cm and refractive index of material is taken to be 1.495. In Figure 3.7, increase in the intensity at desired point during the running of algorithm is shown. In both Figure 3.6 and Figure 3.7, it is obvious that 60% of light can be focused to desired point successfully.

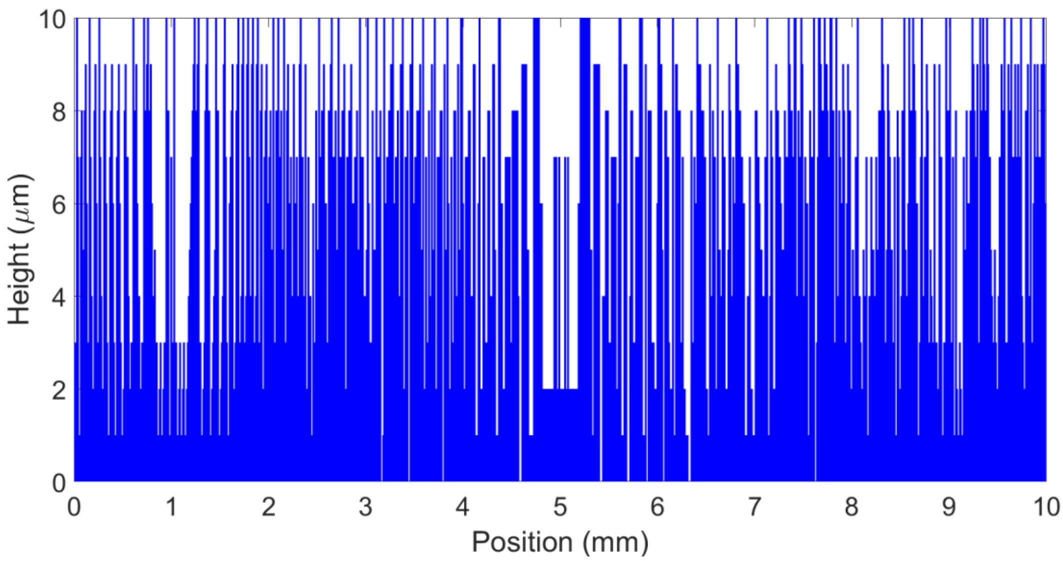

Figure 3.5. Calculated height profile for 1000 pixel, 10 mm length, 10 µm height and refractive index of 1.495.

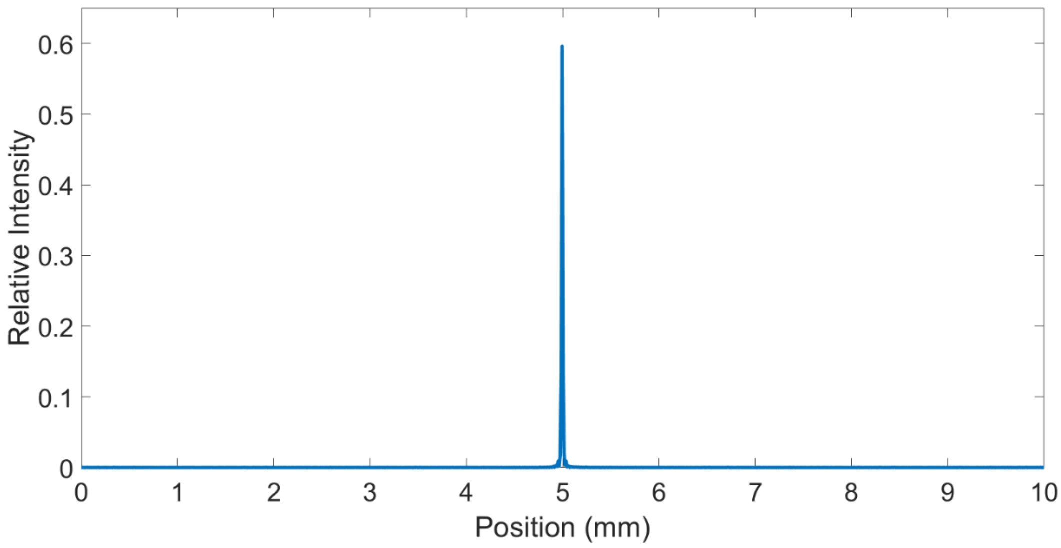

Figure 3.6. Calculated intensity distribution for 400 nm focused to 5 mm away from begining point.

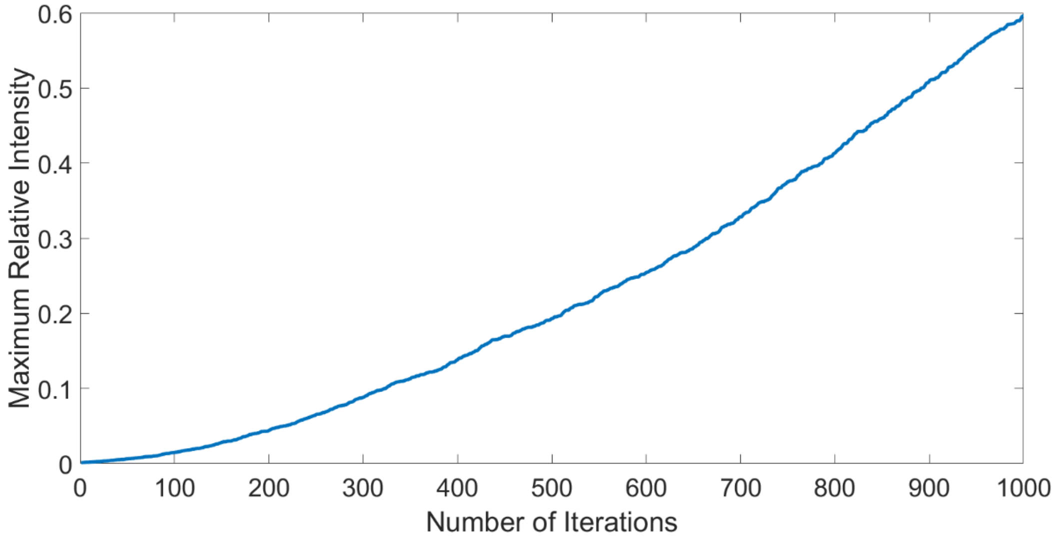

Figure 3.7. Variation of maximum relative intensity by number of iterations.

Instead of a single point, focusing light to a region yields to more effective splitting and is more applicable to solar applications given the size of solar cells. Optimizing height profile to collect light in between 4 and 6 mm results in 86% of total incoming intensity to be focused to desired region. The distribution of intensity for this case is shown in Figure 3.8. The DOE element that we design here simultaneously concentrates two different frequencies to the same region as can be seen in Figure 3.8.

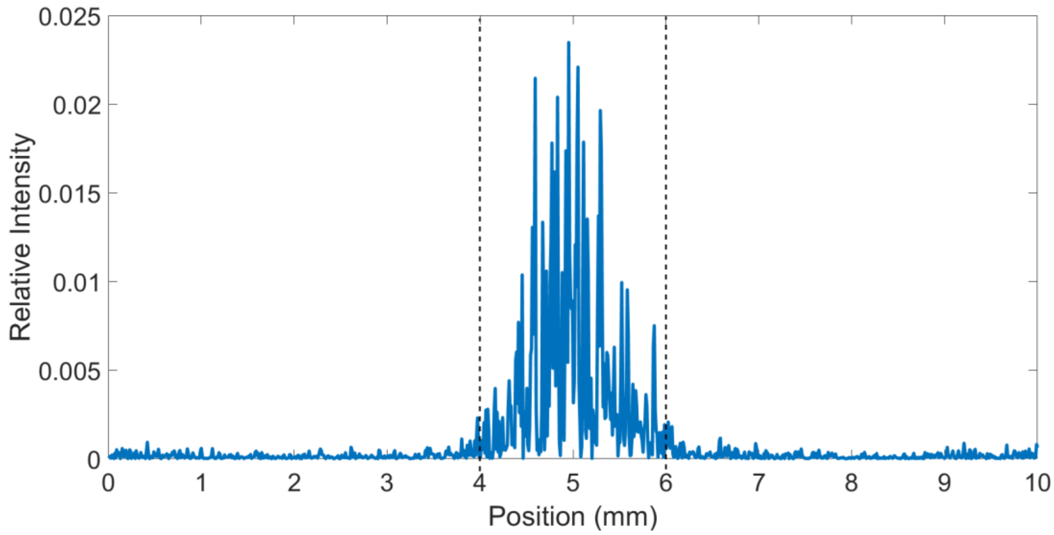

Figure 3.8. Calculated intensity distribution for 400 nm light focused to a region between 4 mm and 6 mm.

3.3 Spectral Splitting of Light via 1D Diffractive Optical Elements

In this section we aim to spectrally split two different frequencies using a single DOE, which is calculated to be as in Figure 3.9. Figure 3.10 shows the output of the DOE that we design for focusing light to two different points at (400 nm and 800 nm). Here the target points are chosen to be 2 mm for 400 nm and 8 mm for 800 nm. 32% of incoming light, 22% of which is 400 nm light while 10% is 800 nm light, is focused to corresponding points. Note that to achieve maximum focusing efficiency, the algorithm repeated five times. In Figure 3.11, it can be seen that after 3000th iterations no change is observed. Given the number of pixel, repetition of the algorithm three times is adequate to reach maximum efficiency. Using our algorithm, we can focus light to different positions as shown in Figure 3.12. This time 31% of incoming light is focused successfully, so for both cases more than 30% of light successfully focused to desired points. For both 400 nm and 800 nm 3% of light falls outside the target region. The reason of this is one of two chosen wavelengths being twofold of the other one. When we run the algorithm for 400 nm and 700 nm, we see that minor peak disappears, as can be seen in Figure 3.13. To consider worst case, we continue our calculations with 800 nm. Lastly, if we run the algorithm to collect 400 nm light between 0 to 5 mm and 800 nm light between 5 to 10 mm as shown in Figure 3.14, we achieve 87% of light collected at desired regions. In order to achieve both spectral splitting and solar concentration, 2-dimensional structures should be optimized.

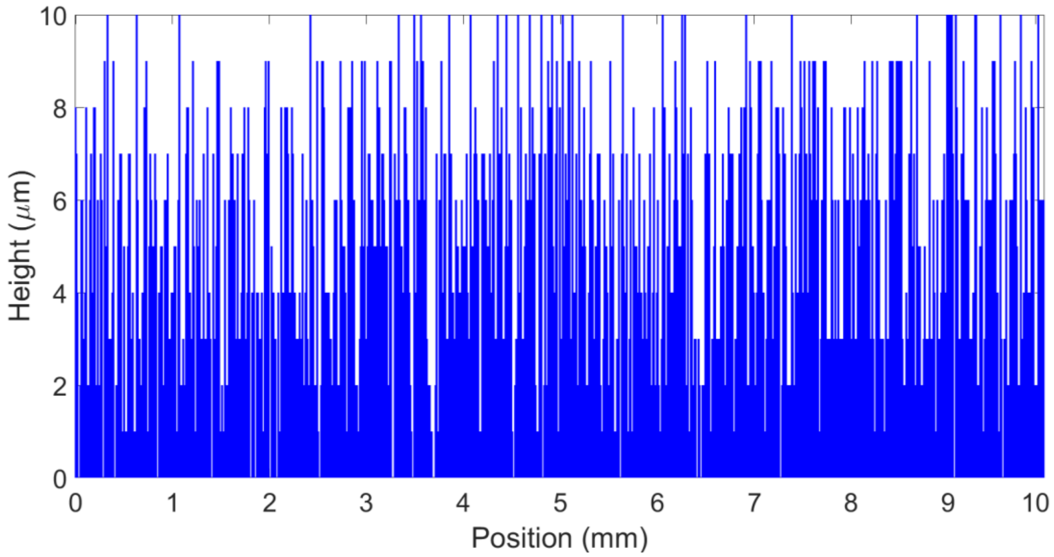

Figure 3.9. Calculated height profile for two wavelength, 1000 pixel, 10 mm length, 10 µm height and refractive index of 1.495.

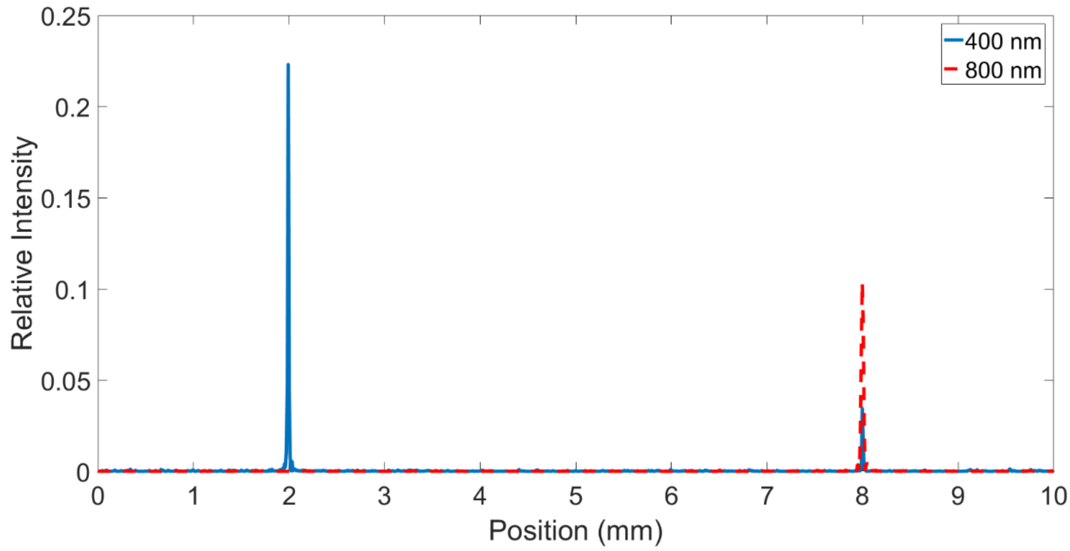

Figure 3.10. Calculated intensity pattern for 400 nm and 800 nm, which are focused to 2 mm and 8 mm respectively.

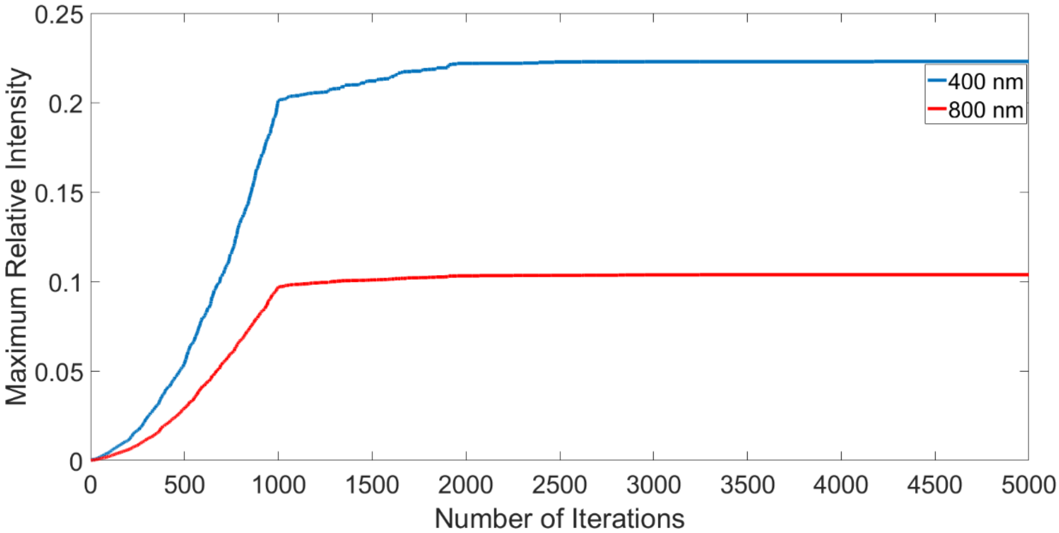

Figure 3.11. Variation of maximum relative intensity by number of iterations.

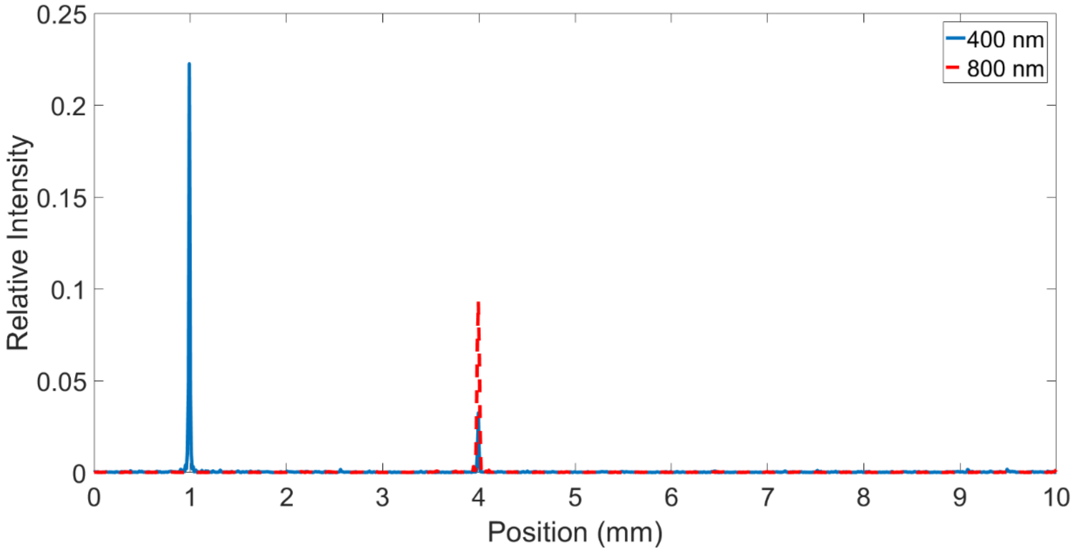

Figure 3.12. Calculated intensity pattern for 400 nm and 800 nm, which are focused to 1 mm and 4 mm respectively.

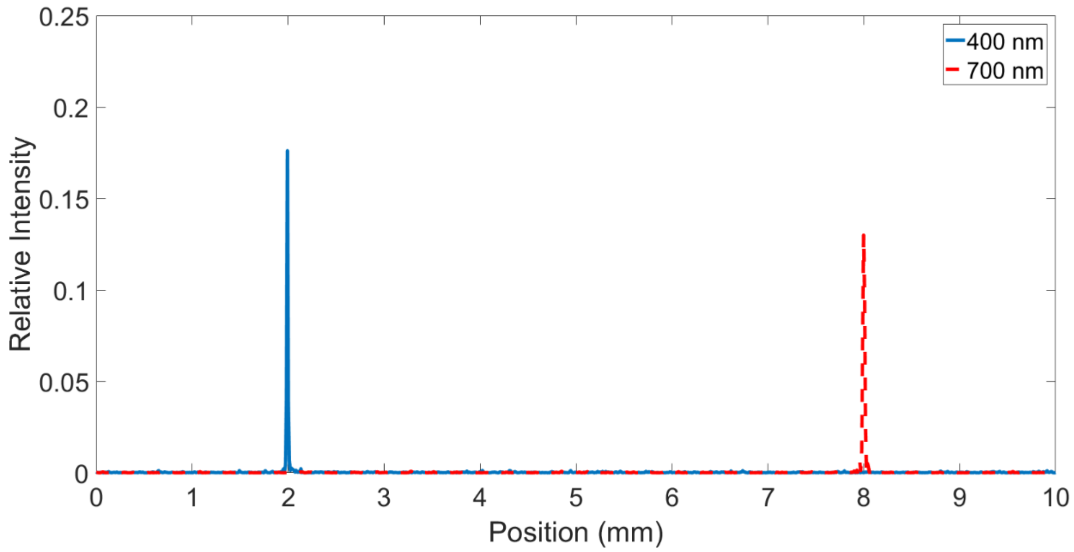

Figure 3.13. Calculated intensity pattern for 400 nm and 700 nm, which are focused to 2 mm and 8 mm respectively.

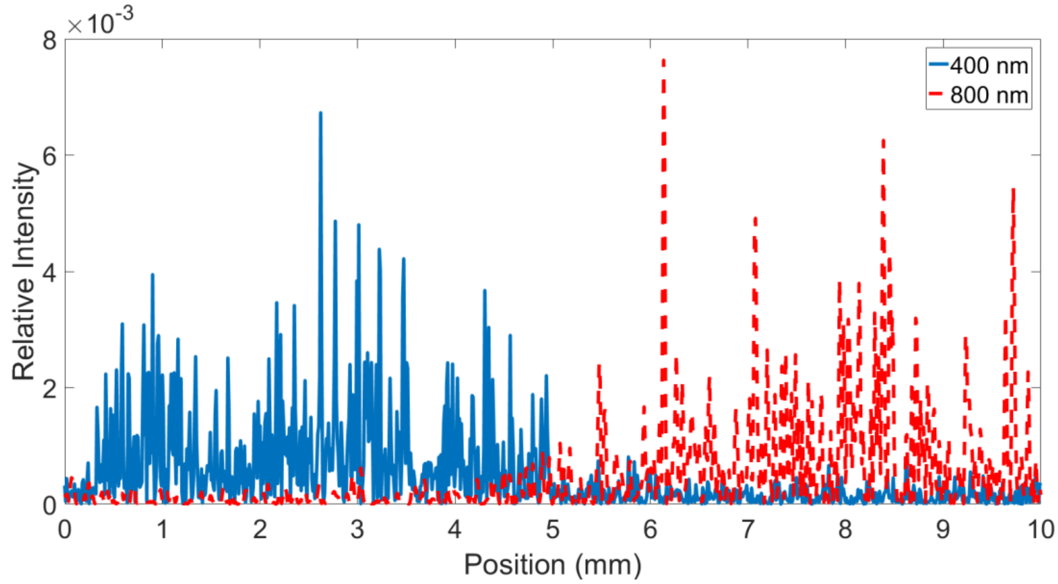

Figure 3.14. Calculated intensity pattern for 400 nm and 800 nm focused to regions. 400 nm is collected between 0 mm and 5 mm, while 800 nm is collected between 5 mm and 10 mm.

3.4 Broadband Spectral Splitting and Concentration of Light via 2D Diffractive Optical Elements

In section 3.2 and 3.3 we demonstrate concentration of light and spectral splitting via DOE, respectively. In this section we combine these two functionalities and design DOE that can achieve solar concentration and spectral splitting simultaneously. For this reason, we develop an algorithm that can optimize DOE in two dimensions. For two dimension, the geometry is taken to be 10 mm × 10 mm and the target positions are chosen to be (2 mm, 8 mm) for 400 nm and (8 mm, 2 mm) for 800 nm. The resolution for the spectral splitter is 35 × 35 pixels and all other values are same with one dimensional case. The resultant height profile is shown in Figure 3.15 and its three

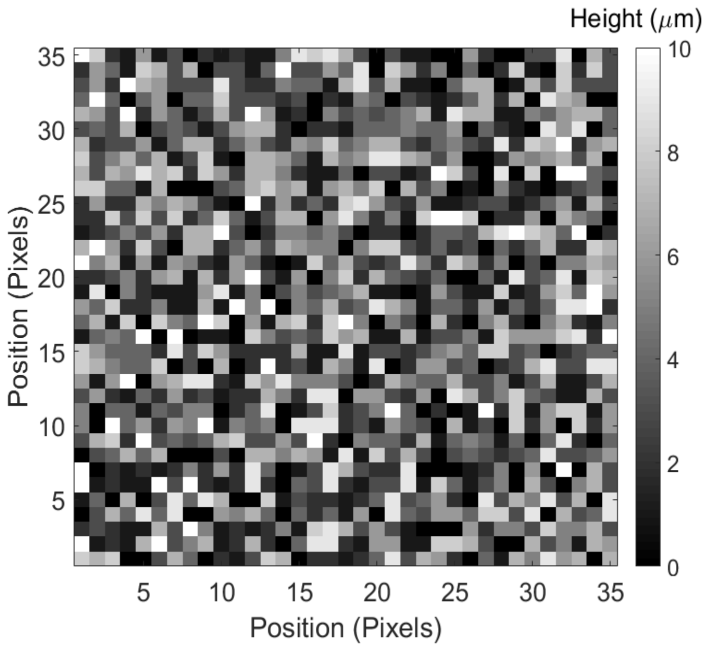

Figure 3.15. Calculated two dimensional height profile with pixel size of 286 μm and refractive index of 1.495.

dimensional view can be seen in Figure 3.16. Intensity pattern expected to be created by this profile is shown in Figure 3.17 for 400 nm and Figure 3.18 for 800 nm. Summation of these two patterns yields to the pattern in Figure 3.19. As can be seen at these three figures, the separation of two wavelengths is obvious and 32% of total intensity is accumulated at desired pixels. For 400 nm, intensity of selected pixel increases from 0.00400% to 21% while for 800 nm it increases from 0.00043% to 11%

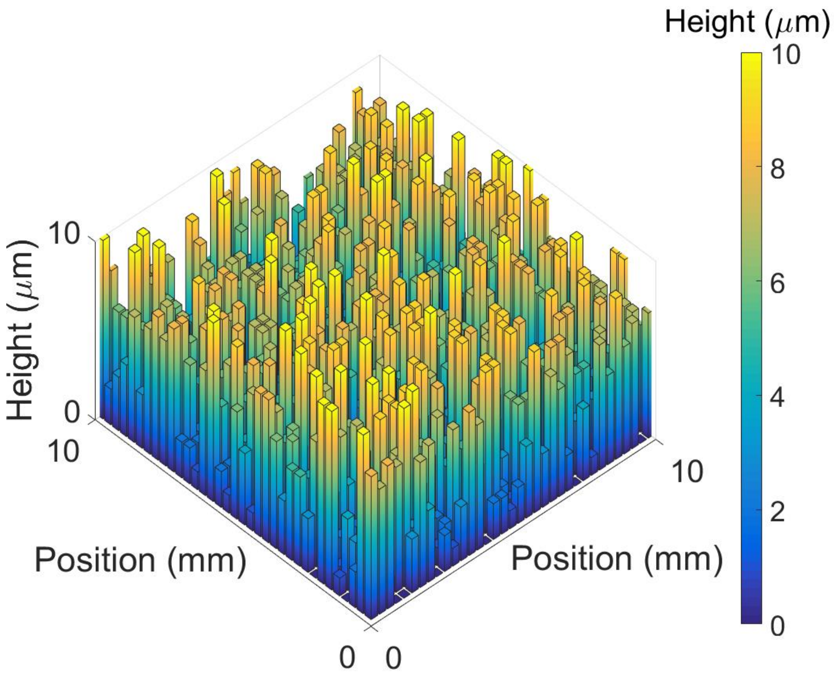

Figure 3.16. 3-Dimensional view of height profile with pixel size of 286 μm and refractive index of 1.495.

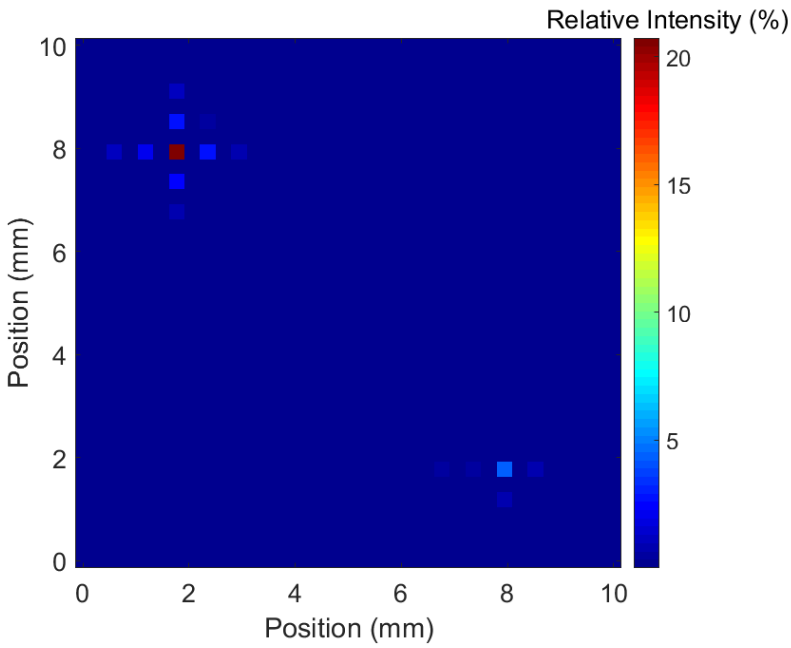

Figure 3.17. Calculated intensity pattern for 400 nm focused to (2 mm, 8 mm).

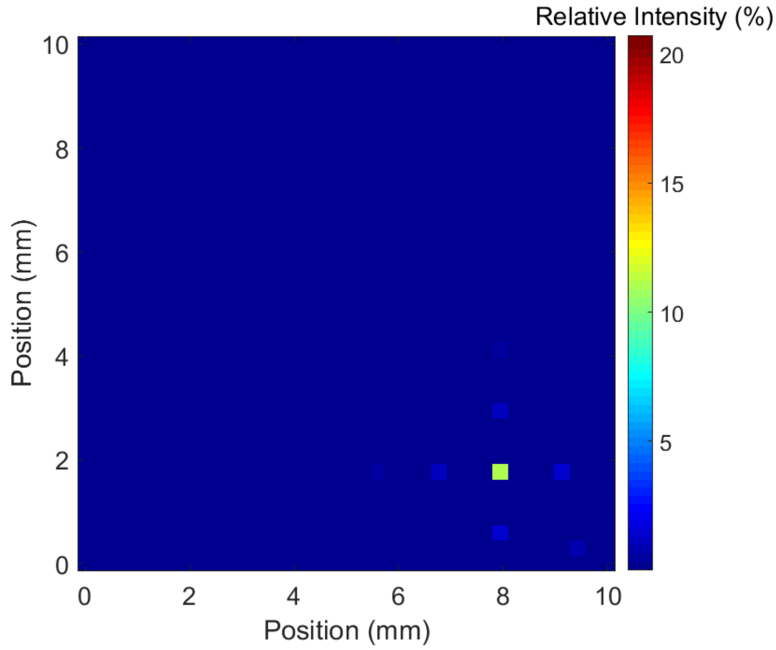

Figure 3.18. Calculated intensity pattern for 800 nm focused to (8 mm, 2 mm).

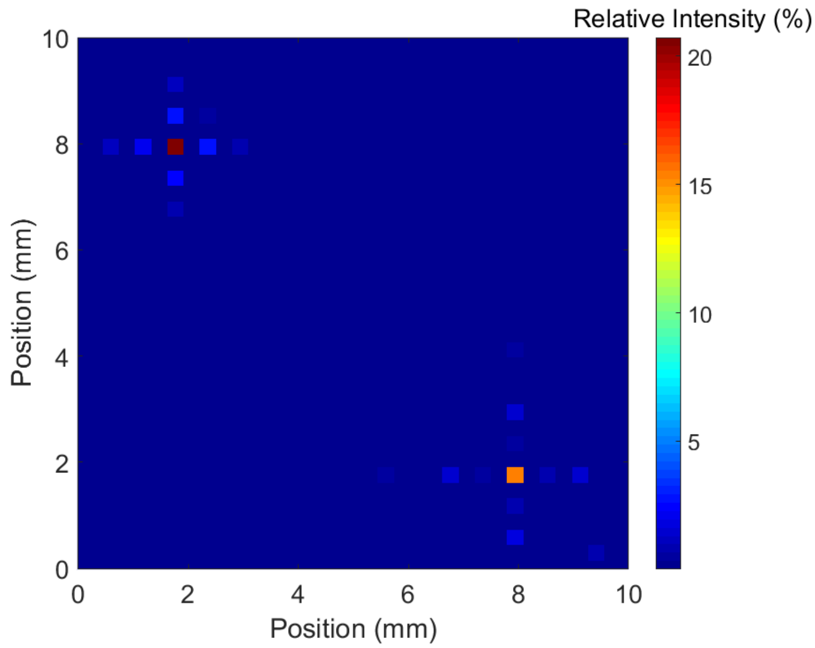

Figure 3.19. Total intensity pattern of 400 nm and 800 nm focused to (2 mm, 8 mm) and (8 mm, 2 mm) respectively.

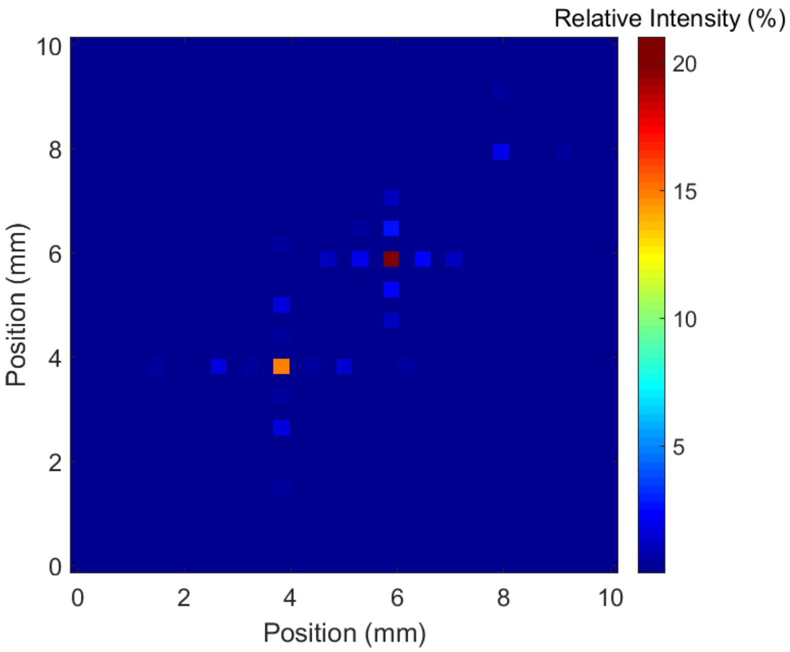

Figure 3.20. Total intensity pattern of 400 nm and 800 nm focused to (6 mm, 6 mm) and (4 mm, 4 mm) respectively.

after optimization. We also obtain results for different positions. In Figure 3.20, we set the target positions to (6 mm, 6 mm) for 400 nm and (4 mm, 4 mm) for 800 nm. According to result, this time 31% of total intensity (20% for 400 nm and 11% for 800 nm) is focused to desired pixels. In this case also, there is erroneous accumulation of 400 nm light at point (4 mm, 4 mm) because of the same reason mentioned for 1D geometry. For two dimensional case, also regions can be targeted light to be focused instead of single points. In Figure 3.21 and Figure 3.22 results of algorithm for two different position sets are shown. For Figure 3.21, light is aimed to collect inside two square corners of which are placed at coordinates of (0 mm, 10 mm), (5 mm, 10 mm), (0 mm, 5 mm), (5 mm, 5 mm) for 400 nm and (5 mm, 5 mm), (10 mm, 5 mm), (5 mm, 0 mm), (10 mm, 0 mm) for 800 nm. For Figure 3.22, the coordinates were set to (0 mm, 5 mm), (5 mm, 5 mm), (0 mm, 0 mm) and (5 mm, 0 mm) for 400 nm and (5 mm, 10 mm), (10 mm, 10 mm), (5 mm, 5 mm) and (10 mm, 5 mm) for 800 nm. In both cases splitting is achieved with total efficiency of more than 70%. The former results in 45% of 400 nm and 26% of 800 nm accumulates at desired regions while for latter case 48% of 400 nm and 25% of 800 nm are focused to desired regions. The efficiency of focusing can be even higher if the resolution increases. After all, it is clear that

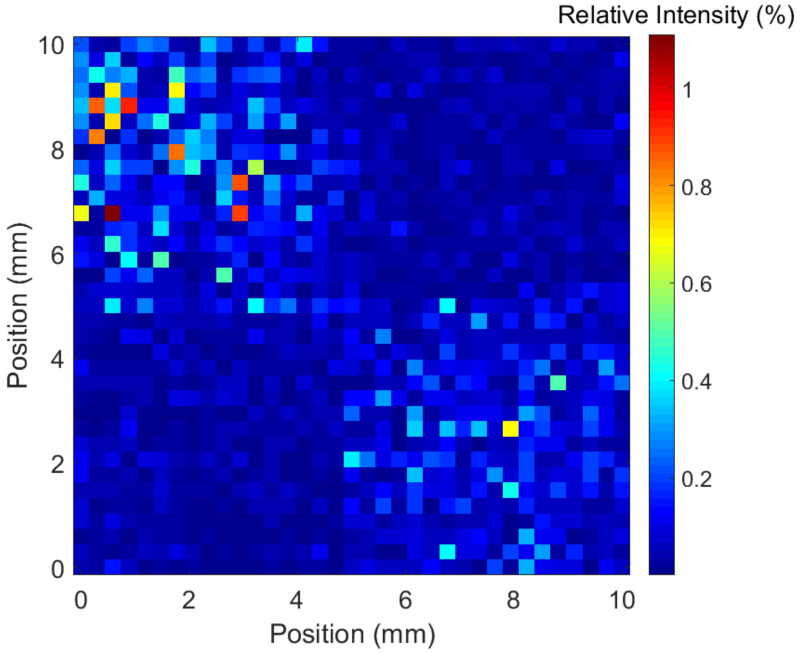

Figure 3.21. Calculated intensity pattern for 400 nm and 800 nm, which are focused to regions corners of which are placed at coordinates of (0 mm, 10 mm), (5 mm, 10 mm), (0 mm, 5 mm), (5 mm, 5 mm) for 400 nm and (5 mm, 5 mm), (10 mm, 5 mm), (5 mm, 0 mm), (10 mm, 0 mm) for 800 nm.

region optimization is much more efficient than point optimization. Besides, it is more useful for solar applications due to its convenience to fabrication processes that employ area detectors.

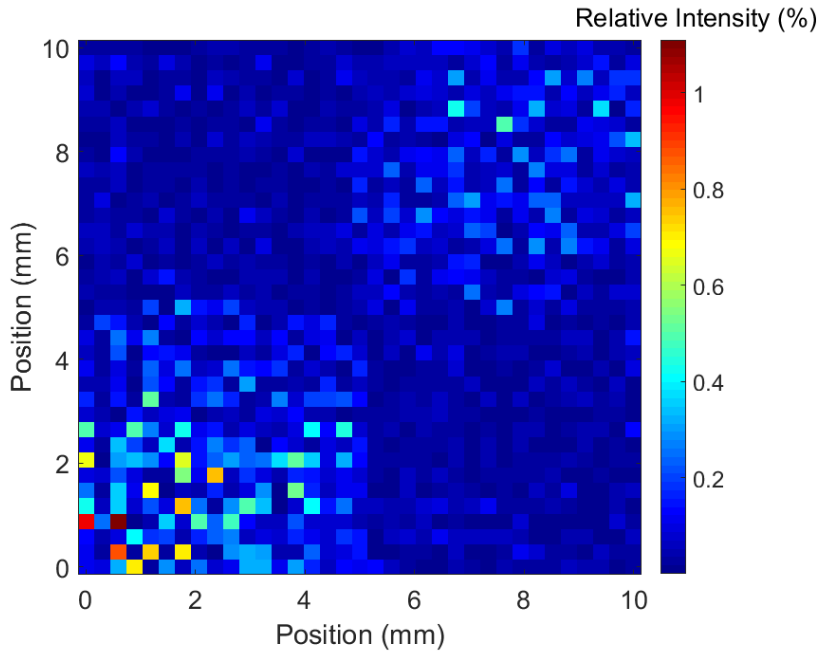

Figure 3.22. Calculated intensity pattern for 400 nm and 800 nm, which are focused to regions corners of which are placed at coordinates (0 mm, 5 mm), (5 mm, 5 mm), (0 mm, 0 mm) and (5 mm, 0 mm) for 400 nm and (5 mm, 10 mm), (10 mm, 10 mm), (5 mm, 5 mm) and (10 mm, 5 mm) for 800 nm.

3.5 Response Change of Height Profile with Angle Variations

A critical constraint for solar cells is change in the angle of incoming solar radiation throughout the day or year. This fact limits the overall efficiency of spectral splitting of DOE's which are optimized for normal incidence. However, it is possible to optimize the structure by also considering different angles. The only difference is that while comparing intensities collected to desired regions, this comparison should also be made for different angles and results are dispatched to "AND" gate. In Figure 3.23, results for 0° to 0.01° for a height profile optimized for both 0° and 0.004° are shown. Unsurprisingly, the results are translated versions of each other due to Fourier relation between angle and position. The total relative intensity of 400 nm light focused properly is 45% for without angle case, and 30% for 0.004°. For 800 nm light, the results are 27% and 12%, respectively.

Here we conclude that structures that are split into two regions vertically are optimal for solar applications. The light stays inside the designed region (left or right half) during the day at different angle of incidence. Our results show that optimizing light to a smaller region inside the designated half is more advantageous since the concentrated light only shifts in position and the total intensity change stays relatively constant. In case the optimization is performed so that the light is split and concentrated to the complete half the change in output intensity as a function of angle would be more drastic. DOE that are optimized in quasi 2 dimensions will suffer more from variations in incidence angle. On the other hand, DOE that we design here enables solar concentration as a result light can be confined inside the targeted area which will shift in position at different angle of incidence while the output is retained.

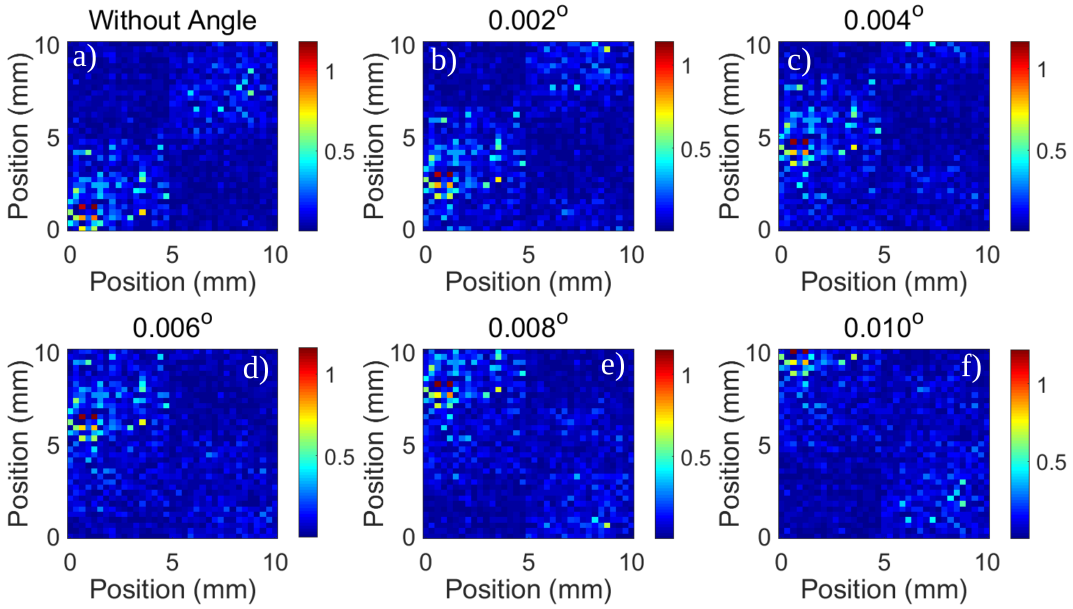

Figure 3.23. Change of intensity pattern with angle. Angles are: a) 0° b) 0.002° c) 0.004° d) 0.006° e) 0.008° f) 0.010°.

CHAPTER 4

CONCLUSION

To conclude with, we examined and analyzed the possible enhancements in spectral splitting and concentrating of sunlight, which has improving effect on solar cells efficiency. Previous works achieved remarkable increase in efficiency by splitting light into different frequencies and sending them to corresponding materials, however, these studies is limited to one dimensional optimization. Our contribution is to expand the works to second dimension by theoretical calculations, and even consider the effect of varied incoming angle. Adding second dimension provides more flexibility for manipulating light and this leads to rise in splitting efficiency. Calculations for varied incoming angle are also promising for optimizing the splitting process by considering possible positions of sun in a whole day. We also come to a conclusion that focusing light to a smaller region rather than half of the plate for example, results in better results for varied incoming angle.

All results we obtained are required to be tested experimentally. The experiments can be conducted by using any structure that provides ability to create two dimensional optical path length patterns. The variance of elements of pattern may be realized through both heights of the structure and refractive index of material, that is to say, electronic devices as spatial light modulators can be utilized as well as fabricated structures with varied thickness. Usage of electronic devices has some extra advantages as enabling real time experiments for finding optimum pattern and even its ability to change pattern after introducing to solar cells. However, they also have some disadvantages as consuming extra energy, higher losses during the splitting process and high cost. Regardless, they provide great opportunity of enhancing solar cells for future of solar energy.

REFERENCES

1. Tobergte, D. R. & Curtis, S. *A History of Thermodynamics*. *Journal of Chemical Information and Modeling* **53,** (2013).

2. Evans, Joanne; Hunt, L. C. *International Handbook on the Economics of Energy*. (Edward Elgard, 2009).

3. Bithas, K. & Kalimeris, P. Revisiting the Energy-Development Link. 5–11 (2016). doi:10.1007/978-3-319-20732-2

4. Nelson, J. *The Physics of Solar Cells* (*Series on Properties of Semiconductor Materials).* (Imperial College Press, 2003).

5. National Renewable Energy Laboratory. (2018). Available at: https://www.nrel.gov/pv/assets/images/efficiency-chart-20180716.jpg.

6. Freundlich, Alexandre; Reinders, Angèle; Sark, Wilfried van; Verlinden, P. *Photovoltaic Solar Energy: From Fundamentals to Applications*. (Wiley, 2017).

7. Kalogirou, S. *Mcevoy's handbook of photovoltaics fundamentals and applications*. (Academic Press, 2018).

8. Kim, G., Domínguez-Caballero, J. a. & Menon, R. Design and analysis of multi-wavelength diffractive optics. *Opt. Express* **20,** 2814 (2012).

9. Gretzki, P. & Gillner, A. Programmable diffractive optic for multi-beam processing: applications and limitations. *Opt. Trapp. Opt. Micromanipulation XIV* 31 (2017). doi:10.1117/12.2274448

10. Mohammad, N., Meem, M., Shen, B., Wang, P. & Menon, R. Broadband imaging with one planar diffractive lens. *Sci. Rep.* **8,** 1–6 (2018).

11. Xie, H., Ren, D., Wang, C., Mao, C. & Yang, L. Design of high-efficiency diffractive optical elements towards ultrafast mid-infrared time-stretched imaging and spectroscopy. *J. Mod. Opt.* **65,** 255–261 (2018).

12. Farn, M. W., Stern, M. B., Veldkamp, W. B. & Medeiros, S. S. Color separation by use of binary optics. *Opt. Lett.* **18,** 1214–6 (1993).

13. Dong, B. Z. *et al.* Design and fabrication of a diffractive phase element for wavelength demultiplexing and spatial focusing simultaneously. *Appl. Opt.* **35,** 6859–64 (1996).

14. Kim, G., Dominguez-Caballero, J. A., Lee, H., Friedman, D. J. & Menon, R. Increased photovoltaic power output via diffractive spectrum separation. *Phys. Rev. Lett.* **110,** 1–5 (2013).

15. Mohammad, N., Wang, P., Friedman, D. J. & Menon, R. Enhancing photovoltaic output power by 3-band spectrum-splitting and concentration

using a diffractive micro-optic. **22,** 1519–1525 (2014).

16. Goodman, J. W. *Introduction to Fourier Optics*. (McGraw-Hill, 1996).

17. Fritts, C. E. On a new form of selenium cell, and some electrical discoveries made by its use. *Am. J. Sci.* **s3-26,** 465–472 (1883).

18. Rappaport, P. The photovoltaic effect and its utilization. *Sol. Energy* **3,** 8–18 (1959).

19. Williams, R. Becquerel photovoltaic effect in binary compounds. *J. Chem. Phys.* **32,** 1505–1514 (1960).

20. Shockley, W. & Queisser, H. J. Detailed balance limit of efficiency of p-n junction solar cells. *J. Appl. Phys.* **32,** 510–519 (1961).

21. De Gennes, P.-G. *Comptes rendus Hebd. des séances l'Académie des Sci. Série B* **275,** 319–321 (1972).

22. Vos, A. De. Detailed balance limit of the efficiency of tandem solar cells. *J. Phys. D. Appl. Phys.* **13,** 839–846 (1980).

23. Gu, B., Yang, G. & Dong, B. General theory for performing an optical transform. *Appl. Opt.* **25,** 3197 (1986).

24. Saleh, B. E. A. & Teich, M. C. *Fundamentals of Photonics*. (John Wiley & Sons, Inc., 1991). doi:10.1002/0471213748

25. Smil, V. *Energy in World History* . (Routledge, 1994).

26. Yang, G., Dong, B., Gu, B., Zhuang, J. & Ersoy, O. K. Gerchberg-Saxton and Yang-Gu algorithms. *Appl. Opt.* **33,** 209–218 (1994).

27. Gu, B. Y., Yang, G. Z., Dong, B. Z., Chang, M. P. & Ersoy, O. K. Diffractive-phase-element design that implements several optical functions. *Appl. Opt.* **34,** 2564–70 (1995).

28. Hecht, E. *Optics*. (Addison-Wesley, 2001).

29. Imenes, A. G. & Mills, D. R. Spectral beam splitting technology for increased conversion efficiency in solar concentrating systems: A review. *Sol. Energy Mater. Sol. Cells* **84,** 19–69 (2004).

30. Messenger, R. A. & Ventre, J. *Photovoltaic systems engineering*. (CRC Press, 2004).

31. Agarwal, G. S., Gbur, G. & Wolf, E. Coherence properties of sunlight. *Opt. Lett.* **29,** 459–461 (2004).

32. Ersoy, O. K. *Diffraction, Fourier Optics and Imaging*. *Wiley Series in Pure and Applied Optics* (Wiley, 2006).

33. Pedrotti, F. L., Pedrotti, L. S. & Pedrotti, L. M. *Introduction to Optics*. (Pearson Education, 2007).

34. Geisz, J. F. *et al.* 40.8% Efficient Inverted Triple-Junction Solar Cell With Two Independently Metamorphic Junctions. *Appl. Phys. Lett.* **93,** 1–4 (2008).

35. Ghatak, A. *Optics*. (McGraw-Hill Education, 2009).

36. Miller, O. D., Yablonovitch, E. & Kurtz, S. R. Strong internal and external luminescence as solar cells approach the Shockley-Queisser limit. *IEEE J. Photovoltaics* **2,** 303–311 (2012).

37. Miller, O. D., Yablonovitch, E. & Kurtz, S. R. Intense internal and external fluorescence as solar cell approach the SQ efficiency limit. *Photovoltaics, IEEE J.* **2,** 1–27 (2012).

38. Mashaal, H., Goldstein, A., Feuermann, D. & Gordon, J. M. First direct measurement of the spatial coherence of sunlight. *Opt. Lett.* **37,** 3516 (2012).

39. Huang, Q. *et al.* Design and fabrication of a diffractive optical element as a spectrum-splitting solar concentrator for lateral multijunction solar cells. *Appl. Opt.* **52,** 2312–9 (2013).

40. Maragliano, C., Chiesa, M. & Stefancich, M. Point-focus spectral splitting solar concentrator for multiple cells concentrating photovoltaic system. *J. Opt. (United Kingdom)* **17,** (2015).

41. Divitt, S. & Novotny, L. Spatial coherence of sunlight and its implications for light management in photovoltaics. *Optica* **2,** 95 (2015).

42. Vorndran, S., Russo, J. M., Wu, Y., Pelaez, S. A. & Kostuk, R. K. Broadband Gerchberg-Saxton algorithm for freeform diffractive spectral filter design. *Opt. Express* **23,** A1512 (2015).

43. Vorndran, S., Russo, J. M., Wu, Y., Pelaez, S. A. & Kostuk, R. K. Broadband Gerchberg-Saxton algorithm for freeform diffractive spectral filter design. *Opt. Express* **23,** A1512 (2015).

44. Albarazanchi, A., Gerard, P., Ambs, P. & Meyrueis, P. Alternative model of a subwavelength diffractive lens proposed for PV Cells Applications. *IEEE Photonics Technol. Lett.* **27,** 1317–1320 (2015).

45. Mackay, M. E. *Solar Energy: An Introduction*. (Oxford University Press, 2015). doi:10.1063/PT.3.3172

46. Khetarpal, D. World Energy Resources: Solar 2016. *World Energy Counc.* 78 (2016).

47. Xiao, T. P. *et al.* Diffractive Spectral-Splitting Optical Element Designed by Adjoint-Based Electromagnetic Optimization and Fabricated by Femtosecond 3D Direct Laser Writing. *ACS Photonics* **3,** 886–894 (2016).

48. Oskolovich, L. E. L. D. *et al.* Multifocal diffractive lens generating several fixed foci at different design wavelengths. **35,** 6859–6864 (2016).

49. Albarazanchi, A. *et al.* Smart multifunction diffractive lens experimental

validation for future PV cell applications. *Opt. Express* **24,** A139 (2016).

50. Maragliano, C. *et al.* Efficiency enhancement in two-cell CIGS photovoltaic system with low-cost optical spectral splitter. *Opt. Express* **24,** A222 (2016).

51. Brown, M., Cox, B. & Treeby, B. Design of multi-frequency acoustic kinoforms. *IEEE Int. Ultrason. Symp. IUS* **244101,** (2017).

52. EIA. International Energy Outlook 2017 Overview. *U.S. Energy Inf. Adm.* **IEO2017,** 143 (2017).

53. Li, J. *et al.* High focusing efficiency or high signal-to-noise ratio diffractive optical element for color separation and light focusing. *Optik (Stuttg).* **138,** 87–94 (2017).

54. International Energy Agency Photovoltaic Power Systems Programme. Snapshot of global photovoltaic markets 2016. 1–16 (2017).

55. Xu, W. Q. *et al.* Simple and universal method in designs of high-efficiency diffractive optical elements for spectrum separation and beam concentration. *Chinese Phys. B* **26,** (2017).

56. REN21. *Renewables 2017: global status report*. *Renewable and Sustainable Energy Reviews* **72,** (2017).

57. Sundaram, S. & Benson, D. *Production Solar Photovoltaic Technology Production Implications for Governance*. (Elsevier, 2016)

APPENDIX

Code for 1-Dimension

```
close all
clear all
tic
position = [2e-3 2e-3; 8e-3 , 8e-3];
sz = 0.01;
px = 10e-6;
M = round(sz/px);
n = 1.495;
u0 = 1;
l = 400e-3;
h_size = 10e-6;
step_size = 1e-6;
step_num = h_size/step_size;
x = 0:sz/(M - 1):sz;
lambda = [400e-9 700e-9];
U_plane = zeros(1, M, size(lambda, 2));

h = ones(M, 1)*step_size;
h1 = h;
for a = 1:size(lambda, 2)
    U_plane(:, :, a) = u0*exp(1i*2*pi.*h1*(n - 1)/lambda(a));
end

h = round(rand(M, 1)*step_num)*step_size;

h1 = h;
h_max = h;
for a = 1:size(lambda, 2)
    U_plane(:, :, a) = u0*exp(1i*2*pi.*h1*(n - 1)/lambda(a));
end

for d = 1:size(lambda, 2)
    for b = 1:M
        U_last1(1, b, d) = 0;
        for c = 1:M
            G(b, c, d) = (1i*lambda(d)*l)^(-
0.5)*exp(1i*2*pi*l/lambda(d))*exp(1i*pi*(c*px -
b*px)^2/(lambda(d)*l));
            U_last1(1, b, d) = U_last1(1, b, d) + G(b, c,
d)*U_plane(1, c, d);
        end
    end
    I1(:, d) = abs(U_last1(:, :, d)).^2/sum(abs(U_last1(:, :,
d)).^2);
end

U_last_max = U_last1;
I_max = I1;
mm = zeros(10,2);
```

```
sayi = 0;
for z = 1:1
for i = 1:M
for j = 0:step_num
    sayi = sayi + 1;
    h(i) = step_size*j;
    for a = 1:size(lambda, 2)
        U_plane(:, :, a) = u0*exp(1i*2*pi.*h*(n - 1)/lambda(a));
    end
for d = 1:size(lambda, 2)
    for b = 1:M
        U_last(1, b, d) = 0;
        for c = 1:M
            G(b, c, d) = (1i*lambda(d)*l)^(-
0.5)*exp(1i*2*pi*l/lambda(d))*exp(1i*pi*(c*px -
b*px)^2/(lambda(d)*l));
            U_last(1, b, d) = U_last(1, b, d) + G(b, c,
d)*U_plane(1, c, d);
        end
    end
    I(:, d) = abs(U_last(:, :, d)).^2/sum(abs(U_last(:, :, d)).^2);
end

sum_max = zeros(1, size(lambda, 2));
sum_last = zeros(1, size(lambda, 2), 1);
for y = 1:size(lambda, 2)
for g = round(position(y, 1)/px):round(position(y, 2)/px)
    sum_max(y) = sum_max(y) + I_max(g, y);
    sum_last(y) = sum_last(y) + I(g, y);
end
end
log = 1;
for y = 1:size(lambda, 2)
if sum_max(y) < sum_last(y) && log == 1
    log = 1;
else
    log = 0;
end
end
if log == 1
    U_last_max = U_last;
    h_max(i) = h(i);
    sum_max = sum_last;
    I_max = I;
else
    h(i) = h_max(i);
end
end
graph(i, z, 1) = sum_max(1);
graph(i, z, 2) = sum_max(2);
end
toc
figure
plot(x, I_max(:, 1)/sum(sum(I_max)))
hold on
plot(x, I_max(:, 2)/sum(sum(I_max)), 'red')
```

```
end
figure
plot(reshape(graph(:,:,1) , [i*z 1]));
hold on
plot(reshape(graph(:,:,2) , [i*z 1]), 'r');
toc
```

Code for 2-Dimension

```
clear all
tic
position(:, :, 1) = [6e-3 6e-3; 6e-3 6e-3];
position(:, :, 2) = [4e-3 4e-3; 4e-3 4e-3];
sz = 0.01;
px = 2.8571e-04;
M = round(sz/px);
n = 1.495;
u0 = 1;
l = 400e-3;
h_size = 10e-6;
step_size = 1e-6;
step_num = h_size/step_size;
x = 0:sz/(M - 1):sz;
lambda = [400e-9 800e-9];
U_plane = zeros(M, M, size(lambda, 2));
U_last1 = zeros(M, M, size(lambda, 2));

h = ones(M, M)*step_size;
h1 = h;

for a = 1:size(lambda, 2)
    U_plane(:, :, a) = u0*exp(1i*2*pi.*h1*(n - 1)/lambda(a));
end

h = round(rand(M, M)*step_num)*step_size;

h1 = h;
h_max = h;
for a = 1:size(lambda, 2)
    U_plane(:, :, a) = u0*exp(1i*2*pi.*h1*(n - 1)/lambda(a));
end

for d = 1:size(lambda, 2)
    for b1 = 1:M %b: output plane
    for b2 = 1:M
        U_last1(b1, b2, d) = 0;
        for c1 = 1:M %c: input plane
            for c2 = 1:M
            G = (1i*lambda(d)*l)^(-
0.5)*exp(1i*2*pi*l/lambda(d))*exp(1i*pi*(px*sqrt((c1 - b1)^2 + (c2 -
b2)^2))^2/(lambda(d)*l));
            U_last1(b1, b2, d) = U_last1(b1, b2, d) + G*U_plane(c1,
c2, d);
            end
```

```
        end
    end
    end
    I1(:, :, d) = abs(U_last1(:, :, d)).^2;
end

U_last_max = U_last1;
I_max = I1;
sum_i_max = sum(sum(sum(I_max)));
mm = zeros(1,2);

sayi = 0;
for z = 1:1
for i1 = 1:M
for i2 = 1:M
for j = 0:step_num
    sayi = sayi + 1;
    h(i1, i2) = step_size*j;
    for a = 1:size(lambda, 2)
        U_plane(:, :, a) = u0*exp(1i*2*pi.*h*(n - 1)/lambda(a));
    end
for d = 1:size(lambda, 2)
    for b1 = 1:M
    for b2 = 1:M
        U_last(b1, b2, d) = 0;
        for c1 = 1:M
            for c2 = 1:M
            G = (1i*lambda(d)*l)^(-
0.5)*exp(1i*2*pi*l/lambda(d))*exp(1i*pi*(px*sqrt((c1 - b1)^2 + (c2 -
b2)^2))^2/(lambda(d)*l));
            U_last(b1, b2, d) = U_last(b1, b2, d) + G*U_plane(c1,
c2, d);
            end
        end
    end
    end
    I(:, :, d) = abs(U_last(:, :, d)).^2;
end
sum_i = sum(sum(sum(I)));
sum_max = zeros(1, size(lambda, 2));
sum_last = zeros(1, size(lambda, 2), 1);
for y = 1:size(lambda, 2)
for g1 = round(position(2, 1, y)/px):round(position(2, 2, y)/px)
    for g2 = round(position(1, 1, y)/px):round(position(1, 2, y)/px)
    sum_max(y) = sum_max(y) + I_max(g1, g2, y)/sum_i_max;
    sum_last(y) = sum_last(y) + I(g1, g2, y)/sum_i;
    end
end
end
log = 1;
for y = 1:size(lambda, 2)
if sum_max(y) < sum_last(y) && log == 1
    log = 1;
else
    log = 0;
end
```

```
end
if log == 1
    U_last_max = U_last;
    h_max(i1, i2) = h(i1, i2);
    sum_max = sum_last;
    I_max = I;
    sum_i_max = sum_i;
else
    h(i1, i2) = h_max(i1, i2);
end
end
graph(i1, i2, z, 1) = sum_max(1);
graph(i1, i2, z, 2) = sum_max(2);
end
end
toc
figure
subplot(1, 2, 1)
imshow(I_max(:, :, 1)/sum_i_max, [])
subplot(1, 2, 2)
imshow(I_max(:, :, 2)/sum_i_max, [])

I_total = (I_max(:, :, 1) + I_max(:, :, 2))/sum_i_max;
figure
imshow(I_total, [])
end
```

Code for 2-Dimensional Angle Optimization

```
clear all
tic
sz = 0.01;
px = 2.8571e-04;
M = round(sz/px);
position(:, :, 1) = [1 (round(M/2) - 1); 1 (round(M/2) - 1)];
position(:, :, 2) = [round(M/2) M; round(M/2) M];
n = 1.495;
u0 = 1;
l = 400e-3;
h_size = 10e-6;
step_size = 1e-6;
step_num = h_size/step_size;
x = 0:sz/(M - 1):sz;
lambda = [400e-9 800e-9];
U_plane = zeros(M, M, size(lambda, 2));
U_last1 = zeros(M, M, size(lambda, 2));
alfa_derece = 0.05;
alfa = pi*alfa_derece/180; h = round(rand(M, M)*step_num)*step_size;
h1 = h;
h_max = h;

for a = 1:size(lambda, 2)
    U_plane(:, :, a) = u0*exp(1i*2*pi.*h1*(n - 1)/lambda(a));
end
for d = 1:size(lambda, 2)
```

```
    for b1 = 1:M
    for b2 = 1:M
        U_last1(b1, b2, d) = 0;
        for c1 = 1:M
            for c2 = 1:M
            G = (1i*lambda(d)*l)^(-
0.5)*exp(1i*2*pi*l/lambda(d))*exp(1i*pi*(px*sqrt((c1 - b1)^2 + (c2 -
b2)^2))^2/(lambda(d)*l));
            U_last1(b1, b2, d) = U_last1(b1, b2, d) + G*U_plane(c1,
c2, d);
            end
        end
    end
    end
    I1(:, :, d) = abs(U_last1(:, :, d)).^2;
end

for s1 = 1:M
    for s2 = 1:M
        h_angle(s1, s2) = h(s1, s2) + (2*s1 - 1)*px*tan(alfa)/2;
    end
end

for d = 1:size(lambda, 2)
    U_p1(:, :, d) = u0*exp(1i*2*pi.*h_angle*(n - 1)/lambda(d));
    for b1 = 1:M
    for b2 = 1:M
        U_last_angle1(b1, b2, d) = 0;
        for c1 = 1:M
            for c2 = 1:M
            G_angle1 = (1i*lambda(d)*l)^(-
0.5)*exp(1i*2*pi*l/lambda(d))*exp(1i*pi*(px*sqrt((c1 - b1)^2 + (c2 -
b2)^2))^2/(lambda(d)*l));
            U_last_angle1(b1, b2, d) = U_last_angle1(b1, b2, d) +
G_angle1*U_p1(c1, c2, d);
            end
        end
    end
    end
    I_angle1(:, :, d) = abs(U_last_angle1(:, :, d)).^2;
end

sum_max = zeros(1, size(lambda, 2), 2);

I_max = I1;
sum_i_max = sum(sum(sum(I_max)));

normalized = I_max/sum_i_max;
sum_max(1, 1, 1) = sum(sum(normalized(position(1, 1, 1):position(1,
2, 1), position(2, 1, 1):position(2, 2, 1), 1)));
sum_max(1, 2, 1) = sum(sum(normalized(position(1, 1, 2):position(1,
2, 2), position(2, 1, 2):position(2, 2, 2), 2)));

I_max_angle = I_angle1;
sum_i_max_angle = sum(sum(sum(I_max_angle)));
```

```
normalized_angle = I_max_angle/sum_i_max_angle;
sum_max(1, 1, 2) = sum(sum(normalized_angle(position(1, 1,
1):position(1, 2, 1), position(2, 1, 1):position(2, 2, 1), 1)));
sum_max(1, 2, 2) = sum(sum(normalized_angle(position(1, 1,
2):position(1, 2, 2), position(2, 1, 2):position(2, 2, 2), 2)));



sayi = 0;
for i1 = 1:M
for i2 = 1:M
for j = 0:step_num
    sayi = sayi + 1;
    h(i1, i2) = step_size*j;
    for a = 1:size(lambda, 2)
        U_plane(:, :, a) = u0*exp(1i*2*pi.*h*(n - 1)/lambda(a));
    end
for d = 1:size(lambda, 2)
    for b1 = 1:M
    for b2 = 1:M
        U_last(b1, b2, d) = 0;
        for c1 = 1:M
            for c2 = 1:M
            G = (1i*lambda(d)*l)^(-
0.5)*exp(1i*2*pi*l/lambda(d))*exp(1i*pi*(px*sqrt((c1 - b1)^2 + (c2 -
b2)^2))^2/(lambda(d)*l));
            U_last(b1, b2, d) = U_last(b1, b2, d) + G*U_plane(c1,
c2, d);
            end
        end
    end
    end
    I(:, :, d) = abs(U_last(:, :, d)).^2;
end


for s1 = 1:M
    for s2 = 1:M
        h_angle(s1, s2) = h_angle(s1, s2) + (2*s1 -
1)*px*tan(alfa)/2;
    end
end

for d = 1:size(lambda, 2)
    U_p(:, :, d) = u0*exp(1i*2*pi.*h_angle*(n - 1)/lambda(d));
    for b1 = 1:M
    for b2 = 1:M
        U_last_angle(b1, b2, d) = 0;
        for c1 = 1:M
            for c2 = 1:M
            G_angle = (1i*lambda(d)*l)^(-
0.5)*exp(1i*2*pi*l/lambda(d))*exp(1i*pi*(px*sqrt((c1 - b1)^2 + (c2 -
b2)^2))^2/(lambda(d)*l));
```

```
            U_last_angle(b1, b2, d) = U_last_angle(b1, b2, d) +
G_angle*U_p(c1, c2, d);
            end
        end
    end
    end
    I_angle(:, :, d) = abs(U_last_angle(:, :, d)).^2;
end


normalized = I_max/sum_i_max;
sum_last(1, 1, 1) = sum(sum(normalized(position(1, 1, 1):position(1,
2, 1), position(2, 1, 1):position(2, 2, 1), 1)));
sum_last(1, 2, 1) = sum(sum(normalized(position(1, 1, 2):position(1,
2, 2), position(2, 1, 2):position(2, 2, 2), 2)));

sum_i_max_angle = sum(sum(sum(I_angle)));

normalized_angle = I_angle/sum_i_max_angle;
sum_last(1, 1, 2) = sum(sum(normalized_angle(position(1, 1,
1):position(1, 2, 1), position(2, 1, 1):position(2, 2, 1), 1)));
sum_last(1, 2, 2) = sum(sum(normalized_angle(position(1, 1,
2):position(1, 2, 2), position(2, 1, 2):position(2, 2, 2), 2)));
save('angle_2D_optimized.mat')
```

Code for Calculating Response of a Height Profile to Different Incoming Angles

```
clear all
load('angle_2D_optimized.mat')
ilk = 0;
son = 0.3;
adim = 0.002;
say = 0;
sum_mat = zeros(round((son - ilk)/adim), 2, 2);
degree = ilk:adim:son;
clear U_last I_max sum_mat
for alfa_derece = ilk:adim:son
say = say + 1;
alfa = pi*alfa_derece/180;
scale_fac = 1;

h_max_angle = imresize(h_max, scale_fac, 'nearest');
for s1 = 1:M*scale_fac
    for s2 = 1:M*scale_fac
        h_max_angle(s1, s2) = h_max_angle(s1, s2) + (2*s1 -
1)*px*tan(alfa)/2;
    end
end

for a = 1:size(lambda, 2)
    U_p(:, :, a) = u0*exp(1i*2*pi.*h_max_angle*(n - 1)/lambda(a));
end

for d = 1:size(lambda, 2)
```

```
    for b1 = 1:M*scale_fac
    for b2 = 1:M*scale_fac
        U_last(b1, b2, d) = 0;
        for c1 = 1:M*scale_fac
            for c2 = 1:M*scale_fac
            G = (1i*lambda(d)*l)^(-
0.5)*exp(1i*2*pi*l/lambda(d))*exp(1i*pi*(px*sqrt((c1 - b1)^2 + (c2 -
b2)^2))^2/(lambda(d)*l));
            U_last(b1, b2, d) = U_last(b1, b2, d) + G*U_p(c1, c2,
d);
            end
        end
    end
    end
    I_max(:, :, d) = abs(U_last(:, :, d)).^2;
end
sum_i_max = sum(sum(sum(I_max)));
pattern(:, :, say, 1) = I_max(:, :, 1)/sum_i_max;
pattern(:, :, say, 2) = I_max(:, :, 2)/sum_i_max;

normalized = I_max(:, :, :)/sum_i_max;
sum_mat(say, 1, 1) = sum(sum(normalized(1:(round(M/2) - 1),
1:(round(M/2) - 1), 1)));
sum_mat(say, 1, 2) = sum(sum(normalized(round(M/2):M, 1:(round(M/2)
- 1), 1)));
sum_mat(say, 1, 3) = sum(sum(normalized(1:(round(M/2) - 1),
round(M/2):M, 1)));
sum_mat(say, 1, 4) = sum(sum(normalized(round(M/2):M,
round(M/2):M,1)));

sum_mat(say, 2, 1) = sum(sum(normalized(1:(round(M/2) - 1),
1:(round(M/2) - 1), 2)));
sum_mat(say, 2, 2) = sum(sum(normalized(round(M/2):M, 1:(round(M/2)
- 1), 2)));
sum_mat(say, 2, 3) = sum(sum(normalized(1:(round(M/2) - 1),
round(M/2):M, 2)));
sum_mat(say, 2, 4) = sum(sum(normalized(round(M/2):M,
round(M/2):M,2)));
end
figure
line1 = plot(degree, sum_mat(:, 1, 1));
hold on
line2 = plot(degree, sum_mat(:, 2, 4), 'r');
hold on
line3 = plot(degree, sum_mat(:, 1, 2), 'g');
hold on
line4 = plot(degree, sum_mat(:, 2, 2), 'y');
```